NTNU – Trondheim
Norwegian University of
Science and Technology

Simulation of viscous Flow around a circular Cylinder with STAR-CCM+

Sunniva Selstad Thingbø

Marine Technology
Submission date: June 2013
Supervisor: Bjørnar Pettersen, IMT

Norwegian University of Science and Technology
Department of Marine Technology

NTNU
Norwegian University of Science and Technology
Department of Marine Technology

MASTER THESIS IN MARINE HYDRODYNAMICS

SPRING 2013

FOR

Stud.techn. Sunniva Selstad Thingbø

SIMULATION OF VISCOUS FLOW AROUND A CIRCULAR CYLINDER WITH STAR-CCM+.
(Simulering av viskøs strømning omkring en sirkulær sylinder med STAR-CCM+.)

The candidate is going to do a CFD simulation of the viscous flow around a circular cylinder for Reynolds number 3900. The case with the cylinder close to a wall (pipeline close to seabottom) shall also be investigated. Large Eddy Simulation (LES) shall be applied to simulate three-dimensional flow.
The software system STAR-CCM+ will be used. The candidate shall demonstrate the use of the program on this application. Detailed analyses where the grid (resolution and distribution) is varied shall be carried out. Important parameters will be chosen in cooperation with the supervisor.
In the thesis the candidate shall present his/hers personal contribution to the resolution of the problem within the scope of the thesis work. Theories and conclusions should be based on mathematical derivation and logic reasoning identifying the various steps in the deduction. The original contribution of the candidate and material taken from other sources shall be clearly defined. Work from other sources shall be properly referenced. The candidate should utilize the existing possibilities for obtaining relevant literature.
The thesis should be organized in a rational manner to give a clear exposition of results, assessments and conclusions. The text should be brief and to the point, with a clear language.

The thesis shall contain the following elements: A text defining the scope, preface, list of contents, summary, main body of thesis, conclusions with recommendations for further work, list of symbols and acronyms, references and appendices. All figures, tables and equations shall be numerated.
It is supposed that Department of Marine Technology, NTNU, can use the results freely in its research work by referring to the student's thesis.
The thesis shall be submitted June 10, 2013, in two copies.

Bjørnar Pettersen
Professor/supervisor

Faglig veileder: PhD student Mia Abrahamsen-Prsic

Preface

This report presents the work done for the Master thesis in the discipline of Marine Hydrodynamics at NTNU, Trondheim. The thesis has been carried out individually in the spring of 2013.

The scope of work has been to study the physics of the cases and apply STAR-CCM+ and Large Eddy Simulations to simulate the flow. A three-dimensional Computational Fluid Dynamics analysis has been carried out for a cylinder with Reynolds number equal to 3900. Two different cases have been studied; a cylinder subjected to steady current and a cylinder in the vicinity of a rigid wall. The main goal was to run analyses for a circular cylinder in viscous flow and compare the results to published studies, as well as understanding the physics involved in the cases. Learning to use the software system STAR-CCM+ for CFD analyses was also important. The thesis work has been very rewarding.

During the semester, much time was spent on the preprocessing part of the analyses. A very challenging part of the thesis was to run the simulations sufficiently fast without reducing the accuracy of the results. The simulations were run on the Vilje supercomputer.

Several persons have been engaged and helped me during the thesis work. I would especially like to thank Professor Bjørnar Pettersen for support and good motivation during the semester. I would also like to thank PhD student Mia Abrahamsen-Prsic for professional guidance with case set-up, involvement in the thesis and for always having an open door and answering all my questions. Without the two of you, this thesis would have never been possible.

Support for the Vilje supercomputer must be thanked for help with reducing the computational time. I would like to thank the support team in CD-adapco for quick responding and help during the semester, and CD-adapco and Michael Glockenmeier for software licence.

Trondheim, June 10, 2013

Sunniva Selstad Thingbø

Summary

In this thesis, three-dimensional modelling of the flow around a circular cylinder is accomplished. Two cases are considered. The first (Case 1) is a cylinder in steady, uniform current subjected to Reynolds number 3900. The second case (Case 2) is a cylinder in the vicinity of a rigid wall, also at Reynolds number 3900. For the second case, both a boundary layer velocity profile (Case 2a) and a uniform inlet velocity profile (Case 2b) is simulated. The gap-to-diameter ratio, e/D, is set to 0.2 for Case 2. Large eddy simulations (LES) with Smagorinsky subgrid scale (SGS) model are applied to simulate the flow. LES have ability to resolve fine structures in the turbulent wake of the cylinder. A mesh convergence study is accomplished for Case 2a.

In the first part of the thesis, the background theory for the case is given in addition to information about the applied pre- and postprocessing tools. In the last part of the thesis, the case set-up is described and the results are presented and discussed. Velocity profiles in the cylinder wake, hydrodynamic values and pressure distribution on the cylinder wall are investigated to give a better understanding of the physics in the cases. The results are compared to published experimental measurements and numerical studies.

For the first case, the results tend to agree well with published research. The software system with LES and the Smagorinsky subgrid scale model does successfully simulate the flow in the boundary layers, the shear layers and the near wake. The results are interesting in the context of flow bifurcation for at cylinder subjected to Reynolds number 3900.

The vortex shedding is suppressed for both Case 2a and Case 2b, as expected. For the cylinder in Case 2a, a decreased drag coefficient is observed when compared to Case 1. This is not observed for the cylinder in Case 2b. The two cases are observed to have an increased mean lift coefficient caused by the vicinity of the wall. However, for Case 2b, the increase is of larger magnitude. This is addressed to the pressure distribution on the cylinder surface. There are also observed differences in the wake statistics for Case 2a and Case 2b. It is concluded that both gap-to-diameter ratio and boundary layer thickness have a significant influence on the flow around a circular cylinder.

Sammendrag (Norwegian summary)

I denne masteroppgaven er tre-dimensjonal modellering av strømning rundt en sirkulær sylinder utført. To forskjellige tilfeller er undersøkt. Tilfelle 1 er en sylinder utsatt for stasjonær, uniform strøm og Reynolds tall 3900. For Tilfelle 2 er sylinderen brakt nær en vegg, også med Reynolds tall 3900. For Tilfelle 2 er både et hastighetsprofil med grensesjikt (Tilfelle 2a) og uniform innstrømning (Tilfelle 2b) simulert. Forholdet mellom gapet og diameteren (e/D) er 0.2 for Tilfelle 2. Large Eddy Simulations (LES) med Smagorinsky subrid scale (SGS) modell er anvendt til å til å simulere strømningen. En mesh-konvergensstudie gjennomført For Case 2a.

Bakgrunnsteorien for tilfellene, samt informasjon om preprosessering og postprosessering er beskrevet i første del av oppgaven. I andre del av oppgaven er oppsett av tilfellene illustrert, og videre er resultatene vist og diskutert. Hydrodynamiske parametere, hastighetsprofiler i waken bak sylinderen og trykkfordeling rundt sylinderveggen er undersøkt for å oppnå en bedre forståelse av fysikken i disse tilfellene. Resultatene er sammenlignet med publiserte numeriske og eksperimentelle studier.

For Tilfelle 1 er resultatene i overenstemmelse med publiserte studier. Programveren STAR-CCM+ med LES og Smagorinsky SGS simulerer strømmen i grensesjiktet, skjærlagene og den nærliggende waken tilfredsstillende. Resultatene er interessante med tanke på diskusjon rundt todeling av strømningen for en sirkulær sylinder utsatt for Reynolds tall 3900.

Som forventet er virvelavløsningen undertrykt for både Tilfelle 2a og Tilfelle 2b. Dersom man sammenligner med resultatene fra Tilfelle 1, kan det sees at for Tilfelle 2a blir dragkoeffisienten mindre. Dette er ikke observert for Tilfelle 2b. Både Tilfelle 2a og Tilfelle 2b oppnår større løftkoeffisient, Tilfelle 2b den største. Dette er sett i sammenheng med trykkfordelingen rundt sylinderen. Det er også observert forskjeller i statistikken fra waken mellom Tilfelle 2a og Tilfelle 2b. Det er konkludert med at både forholdet mellom gapet og diameteren samt grensesjikttykkelsen har signifikat betydning for strømmen rundt en sirkulær sylinder.

Contents

List of Figures

List of Tables

List of symbols and acronyms

$(e/D)_{crit}$	Critical gap ratio
Δt	Time step
Δ	Turbulence filer length scale
δ	Boundary layer thickness
δ_{ij}	The Kronecker delta
ϵ_{ij}	Strain rate tensor
κ	von Karman constant
μ	Dynamic viscosity
μ_t	Subgrid scale viscosity
ν	Kinematic viscosity
ω	Vorticity vector
ρ	density
τ	Shear stress
τ_{ij}	Stress tensor
τ_{ij}^S	Subgrid scale Reynolds stress
$\vec{F}$	Force vector
$\vec{f}$	Applied force per unit volume on fluid particle
$\vec{g}$	Acceleration of gravity
$\vec{V}$	Velocity vector
C_D	Drag coefficient
$C_{L,rms}$	Root mean square of the lift coefficient

C_L	Lift coefficient
C_p	Pressure coefficient
C_S	Smagorinksy model parameter
D	Diameter of the cylinder
dp/dx	Pressure gradient
e	Gap between the cylinder wall and the seabed
F_D	Drag force
F_L	Lift force
f_v	Vortex shedding frequency
h	Enthalpy
k	Thermal conductivity
L	Correlation length
L	Length of cylinder in Z-directions
L_r	Mean recirculation zone length
m	Mass
p_c	Pressure in the free stream
Re	Reynolds number
St	Strouhal number
T_v	Vortex shedding period
u	Velocity component in X-direction
$u(y)$	Function for the velocity profile
u_*	Friction velocity
U_c	Free stream flow velocity
v	Velocity component in Y-direction
z_w	Seabed roughness
2D	Two-dimensional
3D	Three-dimensional
CAD	Computer-aided design
CFD	Computational Fluid Dynamics
DNS	Direct Numerical Simulation

LES Large Eddy Simulation

PIV Particle Image Velocimetry

SGS Subgrid scale

URANS Unsteady Reynolds-Averaged Navier-Stokes

Chapter 1

Introduction and Background

Flow around circular cylinders are an important topic in marine hydrodynamics. Many offshore structures are of cylindrical shape, such as risers and pipelines. The use of these structures have been increased, and they will be used also in the future. It is important to understand the flow field around these structures and the forces acting on them.

The background for this thesis is the projectwork, [Thingbø, 2012]. In the project, the flow around a two-dimensional cylinder in steady current and in shear flow for $Re = 100$ was investigated. In this thesis, all analyses are three dimensional and the flow regime is subcritical and thus turbulent. Large Eddy Simulations (LES) are utilized to simulate the fully three-dimensional flow. LES have ability to study fine structures in the turbulent wake of the cylinder and capture the three-dimensionality of such flow. [Breuer, 1998a; Prsic et al., 2012]

1.1 Cylinder in steady current at Reynolds number 3900

Simulations of flow around a circular cylinder are challenging, and thus verification of the CFD code is important. The benchmark case of flow around a circular cylinder at Reynolds number 3900 has been accomplished. This case is widely documented in the literature. However, according to Lysenko et al. (2012), there is no consensus about the turbulence statistics immediately just behind the obstacle. This classic case encapsulates all the complexity of the topology of the flow by preserving the potentially unstable regions where turbulence is generated. These regions are the boundary layers on the cylinder, the two shear layers delimiting the

recirculation region and the wake. The behaviour of the flow in the wake depends on the state of these regions according to the Reynolds number, see Chapter 2. The case focuses on three-dimensional modelling of flow around a circular cylinder in steady current. The details of the flow around the body and in the near wake are analysed.

The current research for this case is mainly based on LES. Breuer (1998a,b) made a detailed study of the influence of three-dimensional effects, the subgrid scale model, discretization scheme and grid resolution on the quality of LES. Tremblay et al. (2000) carried out a series of LES and compared them to the result of direct numerical simulations (DNS). Wissink and Rodi (2008a) used DNS for Reynolds number 3300, which is in the same flow regime. The flow is therefore considered qualitatively equal. The details of the flow in the near wake was studied. Parnaudeau et al. (2008) compared their own LES results to experimental results obtained by particle image velocimetry (PIV). Ong and Wallace (1996) obtained experimental measurements of the flow behind a circular cylinder by hot-wire and x-ray probe measurements. Franke and Frank (2002) performed a LES simulation for Reynolds number 3900 and compared the results to direct numerical simulations of Ma et al. (2000) and the experiments of Ong and Wallace (1996). Li (2011) also applied LES for flow over a circular cylinder at Reynolds number 3900. Lysenko et al. (2012) recently simulated to flow with Mach number 0.2. The differences between the Smagorinsky subgrid scale (SGS) model and the dynamic k-equation SGS model were investigated. The Mach number is of adequately small magnitude and the flow is this considered to be qualitatively equal.

1.2 Cylinder in the vicinity of a rigid wall at Reynolds number of 3900

Flow around a circular cylinder close to a rigid wall is a topic of high interest in the marine technology research community. Challenges which can be addressed to this problem are for example free-spanning subsea pipelines and marine risers in the vicinity of the seabed. The risers and pipelines are subjected to a continuous strain due to exposure of wind and waves. The safety for the structures can be improved if the flow around them and the forces acting on them are better understood.

When a pipeline is placed on an erodible seabed, scour may occur below the pipe due the flow. This may lead to suspended spans of the pipeline where the pipe is suspended above the seabed with a small gap, usually in the range from O(0.1D) to O(1D). It is therefore important to know what kind of changes that take place in the flow around the pipe and forces acting on it. [Sumer and Fredsøe (1997)]

The case investigated is a pipeline placed above the seabed with a gap, e, between the cylinder surface and the seabed equal to $0.2D$. The case have been split into to subcases, Case 2a and Case 2b. In Case 2a, the flow has a logarithmic inlet velocity profile. For Case 2a, a mesh convergence study has been performed. Case

2b has a uniform velocity profile, i.e it is constant over the inlet boundary. For both sub-cases the Reynolds number is 3900. The physics of the case are investigated through the details of the flow around the body and in the near wake.

Several experimental studies have been carried out to investigate the flow around pipelines close to the seabed in the subcritical flow regime, which ranges from 300 $Re < 3 \cdot 10^5$, see Chapter 2. A wind tunnel was used by among others Lei et al. (1999) and Zdravkovich (1985). Particle image velocimetry (PIV) is also used, e.g by Oner et al. (2008), Price et al. (2002) and Wang and Tan (2008). None of the experiments were performed with the exact same Reynolds number. However, the flow range is the same, and the thus the flow is considered qualitatively equal.

Numerical studies have been carried out by among others Ong et al. (2008), Ong et al. (2010), Sarkar and Sarkar (2010), Lei et al. (2000) and Abrahamsen-Prsic et al. (2013). None of the numerical studies are performed for Reynolds number 3900, but again the flow regime is the same. Ong et al. (2008, 2010) performed a two-dimensional analysis using the Unsteady Reynolds-Averaged Navier-Stokes (URANS) and a $k - \epsilon$ turbulence model. Lei et al. (2000) used a two-dimensional finite difference method. Sarkar and Sarkar (2010) simulated the flow using three-dimensional LES analyses and concluded that the results were in good agreement with those obtained by Price et al. (2002). LES have not been applied in the same extent for a cylinder close to a rigid wall as it has for a cylinder in steady, infinite current. However, it is considered promising based on the previous mentioned studies. The results obtained for Case 2 are compared to results obtained for Case 1 and to previous research.

1.3 Thesis Overview

The general setup of a simulation in STAR-CCM+ was described in [Thingbø, 2012], and will therefore not be explained further in the thesis. Chapter 2 describes the background theory for the cases. Chapter 3 briefly describes the numerical method, i.e the Large Eddy Simulations and the Smagorinsky SGS model. Chapter 4 gives a short description of the grid generation tool applied in STAR-CCM+ and the physics of the applied boundary conditions. Chapter 5 describe the postprocessing tools which are used in STAR-CCM+ to obtain the presented results. The strategy for obtaining a sufficient computational time is described in Chapter 6. Chapter 7 and Chapter 8 describes the set-up of Case 1 and Case 2 respectively. The results obtained are discussed in Chapter 9. A review of STAR-CCM+ is given in Chapter 10. Finally the conclusion is evaluated in Chapter 11 and suggestions to further work are given in Chapter 12.

Chapter 2

Background Theory

2.1 Flow Regime

Theory about flow regime is found in [Sumer and Fredsøe, 1997]. The flow regime around a smooth circular cylinder in infinite fluid is described by the non-dimensional Reynolds number:

$$Re = \frac{U_c D}{\nu} = \frac{U_c D}{\mu/\rho} \tag{2.1}$$

where U_c is the flow velocity, D is the diameter of the cylinder, ν is the kinematic viscosity, μ is the dynamic viscosity and ρ is the density. When the Reynolds number is increased from zero, the flow undergoes great changes. The wake will extend over a distance comparable to the cylinder diameter D, and the boundary layer extends over a very small thickness δ (small compared to D).

For very small values of Re, there is no separation, separation will occurs for $Re \geq 5$. For $5 < Re < 40$ a fixed pair of vortices forms in the wake of the cylinder, and the length of the vortices will increase with increasing Re. When the Reynolds number is further increased, the wake becomes unstable and at $Re > 40$ vortex shedding begins. This is a phenomena where vortices are shed alternately at either side of the cylinder at with a frequency, f_v. This means that the wake will look like a vortex street. For $Re \leq 189$ the vortex shedding is laminar and two-dimensional, meaning it does not vary in the spanwise direction. For $Re > 189$ the vortex shedding becomes three-dimensional. With a further increase in Re, transition to turbulence occur in the wake region. This region of transition will move towards the cylinder as Re is increased in the range $200 < Re < 300$. The vortices are shed in cells in the spanwise direction for all $Re > 300$, and the wake is completely turbulent.

For the flow regime, 300 $Re < 3 \cdot 10^5$, the boundary layer over the cylinder surface remains laminar. This flow regime is called the subcritical flow regime.

In the range $3 \cdot 10^5 < Re < 3.5 \cdot 10^5$ the boundary layer becomes turbulent at the separation point, but this occurs only at one side of the cylinder. This means that the boundary layer separation is turbulent on one side of the cylinder and laminar on the other. This flow regime is called the critical (or lower transition) flow regime. Because of the asymmetry, the mean lift on the cylinder will be non-zero. However, the side at which the separation is turbulent may switch between the two sides occasionally, so that the lift force may change direction.

For $3.5 \cdot 10^5 Re < 1.5 \cdot 10^6$ the flow regime is the supercritical flow regime. Here, the boundary layer separation is turbulent on both sides of the cylinder. The region of transition to turbulence is located somewhere between the stagnation point and the separation point.

The boundary layer becomes fully turbulent on one side of the cylinder when Re reaches about $1.5 \cdot 10^6$. Hence, in this flow regime the boundary layer is completely turbulent on one side of the cylinder and partly laminar and partly turbulent on the other side. This flow regime is called the upper-transition flow regime, and it remains for $Re < 4.5 \cdot 10^6$.

Finally, for $Re > 4.5 \cdot 10^6$, the boundary layer over the cylinder is virtually turbulent everywhere. This flow regime is called the transcritical flow regime. One should note that there is no general consensus regarding the terminology in relation to the described flow regimes and also where they occur.

2.2 Vortex Shedding

Theory for vortex shedding is found in [Sumer and Fredsøe, 1997]. When $Re > 40$ the boundary layer over the cylinder surface will separate due to the adverse pressure gradient. This pressure gradient arises because of the divergent environment of the flow at the rear side of the cylinder. The result of this is a shear layer. The boundary layer along the cylinder contains a significant amount of vorticity. The vorticity will continue into the shear layer downstream of the separation point and cause the shear layer to roll up into a vortex with a sign identical to that of the incoming vorticity. This is illustrated in Figure 2.1a.

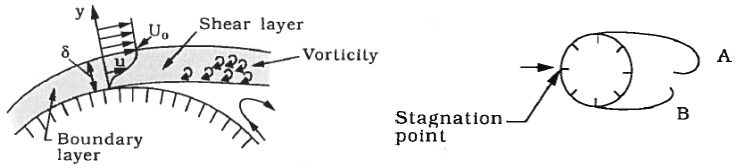

(a) Detailed picture of flow near separation

(b) Beginning of vortex shedding

Figure 2.1: The boundary layer, the shear layer downstream of the cylinder and the beginning of the vortex shedding is illustrated, from [Sumer and Fredsøe, 1997]

Point of Separation

If the momentum equation (Eq. A.19) is applied at the wall, where $u = v = 0$, then

$$\left.\frac{\partial^2 u}{\partial y^2}\right|_{y=0} = \frac{1}{\mu}\frac{dp}{dx} \tag{2.2}$$

Figure 2.2 shows that a positive pressure gradient $dp/dx > 0$ makes the velocity profile more and more S-shaped. The wall shear stress reduces to zero (the separation point), causing backflow and at the same time, the boundary layer becomes thicker. [White, 2006]

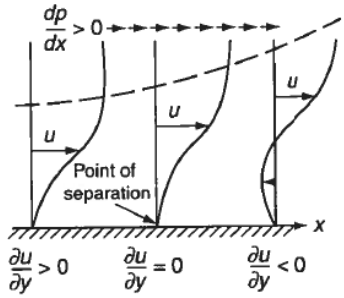

Figure 2.2: Boundary layer and point of separation [White, 2006]

Vorticity

The vorticity vector $\vec{\omega} = \text{curl}\vec{V}$, is a measure of rotational effects, being equal to twice the local angular velocity of a fluid element. If the vorticity is equal to zero,

the flow is irrotational. The vorticity is by White (2006) defined

$$\vec{\omega} = \text{curl}\vec{V} = \vec{\nabla} \times \vec{V} = \begin{vmatrix} \vec{i} & \vec{j} & \vec{k} \\ \frac{\partial}{\partial x} & \frac{\partial}{\partial y} & \frac{\partial}{\partial z} \\ u & v & w \end{vmatrix} \tag{2.3}$$

$$= \left(\frac{\partial w}{\partial y} - \frac{\partial v}{\partial z}\right)\vec{i} - \left(\frac{\partial w}{\partial x} - \frac{\partial u}{\partial z}\right)\vec{j} + \left(\frac{\partial v}{\partial x} - \frac{\partial u}{\partial y}\right)\vec{k}$$

2.2.1 The Mechanism of Vortex Shedding

Theory for vortex shedding is found in [Sumer and Fredsøe, 1997]. The mechanism of vortex shedding can be described in the following way. This is described by using Figure 2.1a and Figure 2.3. When the larger vortex becomes strong enough, it will draw the opposite vortex across the wake. This is sketched in Figure 2.3a. The vorticity in Vortex A is in the clockwise direction, while the vorticity in Vortex B is in the opposite direction. The vorticity with opposite sign (from Vortex B) will cut off the further supply of vorticity to Vortex A from its boundary layer. When this occurs, Vortex A is shed. Now Vortex A is a free vortex and will be convected downstream of the cylinder.

(a) Vortex B is drwan across the wake before Vortex A is shed

(b) Vortex C is drwan across the wake before Vortex B is shed

Figure 2.3: Illustration of vortex shedding from [Sumer and Fredsøe, 1997]

There will now be formed a new vortex at the side of the cylinder where Vortex A was located, named Vortex C. Vortex B will now have the same role as Vortex A had. It will grow in size and strength and draw Vortex C across the wake until it is shed, and Vortex B is free, see figure 2.3b. This alternating vortex shedding will continue to occur between the two sides of the cylinder. The vortex shedding occurs only when the shear layers interact with each other.

2.2.2 Vortex-Shedding Frequency

Theory for vortex shedding is found in [Sumer and Fredsøe, 1997]. To find the Strouhal number St, the vortex shedding period, T_v was found from the plot for the lift coefficient. It can also be found from the oscillating pressure or velocities in a probe in the wake near the cylinder.

The vortex shedding frequency, f_v is given by

$$f_v = \frac{1}{T_v} \tag{2.4}$$

The vortex shedding frequency can be normalized with the flow velocity U_c and the cylinder diameter D. This is called the Strouhal number and is calculated by the formula

$$St = \frac{f_v D}{U_c} \tag{2.5}$$

The Strouhal number varies with the Reynolds number

$$St = St(Re) \tag{2.6}$$

Figure 2.6 illustrates how the Strouhal number varies with Reynolds number.

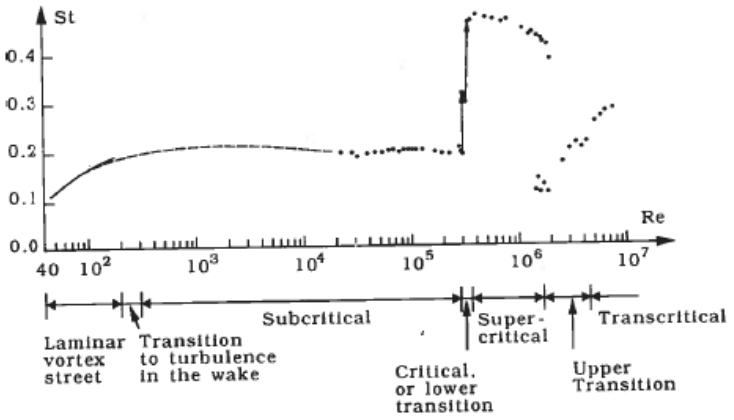

Figure 2.4: Strohal number for a smooth circular cylinder. Different curve types (solid, dashed, dots) are from different experiments. The figure is found in [Sumer and Fredsøe, 1997]

From Figure 2.6, one can see that the Strouhal number is approximately equal to 0.1 when the vortex shedding first begins, at $Re = 40$. It increases gradually when Re is increased until it remains approximately constant at $Re \approx 300$, which is the lower end of the subcritical flow regime. This value of the Strouhal number remains throughout the subcritical range.

It can be seen from Figure 2.6 that the Strouhal number experiences as sudden jump in value at $Re = 3 - 3.5 \cdot 10^5$, which is called the critical range of Re. Here, the Strouhal number has a value of about 0.45. This high value of St is remained for a large part of the supercritical Re range, but it decreases slightly with increasing Re. The reason for the sudden jump in Strouhal number is that boundary layer on both sides of the cylinder is turbulent at the separation point. The result is that the separation point moves downstream. This means that the alternating vortices will interact with each other at a faster rate, meaning the vortex shedding frequency increases. This leads to the increasing Strouhal number.

2.3 Effect of Wall Proximity

According to Sumer and Fredsøe (1997), a number of changes occur in the flow when a pipeline is places close to the seabed. They can be summarized:

1. Vortex shedding is suppressed for the gap ratio values smaller than about $e/D < 0.3$. Here, e is the gap between the cylinder surface and the seabed.
2. The stagnation point moves to a lover angular position, as demonstrated in Figure 2.5. This can easily be seen from the pressure measurements around the cylinder wall and is demonstrated in Figure 2.8.
3. Also, the angular position of the separation points changes. The separation point at the free-stream side of the cylinder moves upstream, and the separation side on the seabed side moves downstream, as shown in Figure 2.5.
4. The suction is larger on the free-stream side of the cylinder than on the seabed side. This disappears when the cylinder is placed away from the seabed, the symmetry is then restored.

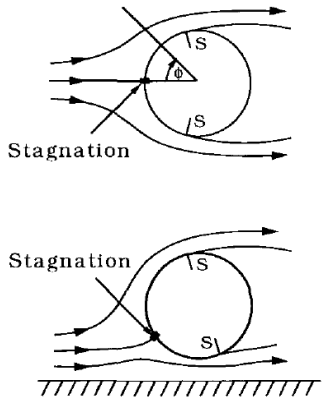

Figure 2.5: Flow around a free cylinder (upper) and a near-wall cylinder (lower). S = separation points. Figure found in [Sumer and Fredsøe, 1997]

The suppression of the vortex shedding is linked with the asymmetry in the development of the vortices on the two sides of the cylinder. Because the vortex on the free-stream side of the cylinder grows larger and stronger than the vortex on the seabed side, the interaction between the two vortices is largely inhibited. For small e/D it is totally inhibited. This will result in partly or complete suppression of the regular vortex shedding. [Sumer and Fredsøe, 1997]

If the vortex shedding exists for a cylinder with a gap e/D, measurements show that the shedding frequency tends to increase (slightly) with decreasing gap ratio. The slight increase in Strouhal frequency may be attributed to the fact that the pressure of the seabed causes a seabed-side vortex to be former closer to the free-stream-side vortex. The result is that the two vortices interact at a faster rate, leading to a higher St frequency. [Sumer and Fredsøe, 1997]

2.4 Forces on a Cylinder in Steady Current

The following theory is found in [Sumer and Fredsøe, 1997]. A force will act a cylinder in steady current. There are two contributions to this force: one from pressure and one from friction. The total *in-line* force, the mean drag, is a sum of the in-line mean pressure force and the in-line mean friction force. The same applies for the mean *cross-flow* force, the lift force, only that the contributes act in the cross-flow direction.

For $Re > 40$, due to the periodic vortex shedding, the pressure will also have periodic change, and thus also the force components will have a periodic variation. Figure 2.6 shows how the forces change with time. The drag force changes period-

ically with time and is oscillating around a mean value; the mean drag. The other force is the oscillating lift force, which also is periodically changing. However, this force has a mean value equal to zero due to the symmetry of the flow.

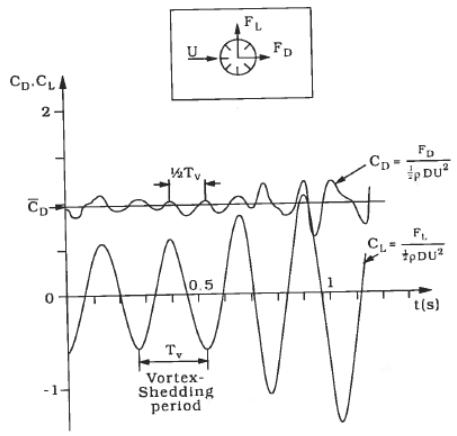

Figure 2.6: Drag force coefficient and lift force coefficient obtained from the measured pressure distribution, found in [Sumer and Fredsøe, 1997]

2.4.1 Oscillating Drag and Lift

The upward lift is associated with the growth of the vortex at the lower edge of the cylinder, and the downward lift is associated with growth of the vortex at the upper edge of the cylinder. Both vortices gives an increase in the drag force. The lift force of the cylinder will oscillate with the vortex shedding frequency f_v, while the drag force will oscillate with the twice of that frequency. The lift coefficient and drag coefficient are by Sumer and Fredsøe (1997) defined as follows:

$$C_D = \frac{F_D}{\frac{1}{2}\rho U_c^2 DL} \tag{2.7}$$

and

$$C_L = \frac{F_L}{\frac{1}{2}\rho U_c^2 DL} \tag{2.8}$$

Here F_D is the drag force, F_L is the lift force, ρ is the water density, U_c is the incoming uniform flow velocity, D is the cylinder diameter and L is the length of the cylinder in Z-direction.

The root mean square (RMS) value for the lift coefficient, is defined $C_{L,rms} = \sqrt{\overline{C_L'^2}}$, where C_L' is the distance to the maximum value for C_L (top point) in each shedding period.

2.4.2 The pressure coefficient

The pressure coefficient gives the variations in the pressure distribution of the cylinder, and is by CD-adapco (2013) given

$$C_p = \frac{p - p_c}{\frac{1}{2}\rho U_c^2} \tag{2.9}$$

Where ρ is the water density, U_c is the incoming uniform flow velocity, and p_c is the pressure in the free stream. In the analyses, p_c is set equal to zero.

2.5 Forces on a Cylinder close to the Seabed

The changes in the flow for a cylinder close to the seabed, will affect the forces acting on it. Theory is found in [Sumer and Fredsøe, 1997].

2.5.1 Drag Force on a Cylinder Near a Plane Wall

For the drag force, the general trend is that the drag coefficient decreases with decreasing gap ratio near the wall. The averaging operator is denoted $\langle\rangle$ One characteristic point in the variation of $\langle C_D \rangle$ with respect to e/D is that $\langle C_D \rangle$ increases in a monotonous manner with increasing e/D up to a certain value of e/D. This behaviour has been linked to the thickness of the boundary layer of the approaching flow. For gap ratio of such a value that the cylinder is fully embedded in the potential flow, the drag $\langle C_D \rangle$ is constant. For values smaller of e/D, so the cylinder is embedded partly in the potential flow and partly in the boundary layer for the incoming flow, the value for $\langle C_D \rangle$ is increasing with increasing e/D. [Sumer and Fredsøe, 1997]

2.5.2 Lift Force on a Cylinder Near a Plane Wall

Because the mean flow around a near-wall cylinder is not symmetric, the mean lift force is non-zero. Figure 2.8 shows that for a cylinder at $e/D = 1$, the flow is almost symmetric, and so the mean mean lift force is practically zero. This symmetry clearly disappears for $e/D = 0.1$ and $e/D = 0$. This results in a non-zero mean lift force acting on the cylinder. One can see from the figure that the direction of the lift force is away from the wall. For $e/D = 0.2 - 0.3$ the lift force fairly small, but

if the gap ratio is decreased it increases tremendously. This is as earlier mentioned because the stagnation point moves to a lower angular position and the suction on the cylinder becomes larger and larger with decreasing gaps. The combination of this results in larger and larger lift forces as the gap is decreased. The effect of shear-flow contra uniform flow is illustrated in Figure 2.7. [Sumer and Fredsøe, 1997]

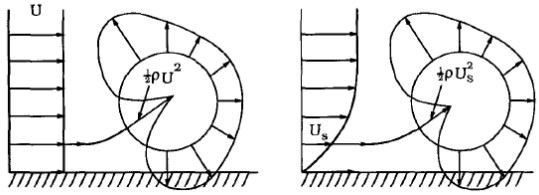

Figure 2.7: Comparison of shear-free and shear flow. The stagnation pressure decreases in the shear flow case. Figure found in [Sumer and Fredsøe, 1997]

When the approaching flow is a shear flow, $\langle C_L \rangle$ undergoes a substantial drop for very small e/D. This can be linked to the change in the stagnation point. The stagnation point will not move significantly because of the shear flow. However, the stagnation pressure is reduced with the introduction of shear compared to the case with uniform flow. When e/D is extremely small, more and more fluid will be forced to pass over the cylinder, which will lead to larger and larger suction pressure on the free-stream side of the cylinder. This mean that the suction pressure on the cylinder surface will be largest when the cylinder is sitting on the wall. This effect may restore the lift force in the shear-flow compared to the uniform flow.

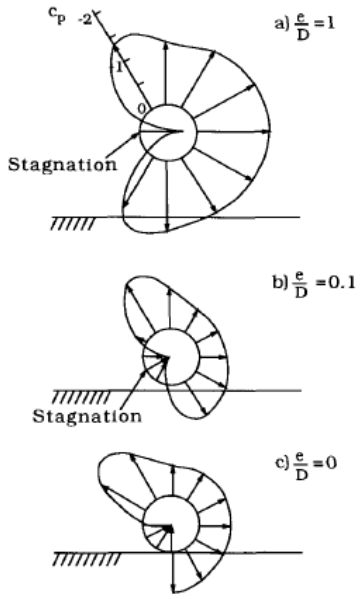

Figure 2.8: Pressure distribution on a cylinder close to a seabed as a function of e/D, found in [Sumer and Fredsøe, 1997]

2.5.3 Oscillating Drag and Lift on a Cylinder Near a Plane Wall

When the gap ratio is smaller then about 0.3, the oscillating lift force will cease to exist, simply because the vortex shedding is suppressed . When e/D is larger than 0.3, but still small, the oscillating lift will be influenced by the proximity of the wall. The oscillating lift force will become weaker and weaker with decreasing e/D. In Figure 2.9 from [Sumer and Fredsøe, 1997], the vortex shedding induced oscillating lift is compared with the mean lift caused by the wall proximity. The C_L coefficient plotted in the figure representing the vortex-induced oscillating lift is the mean lift coefficient associated with the maximum value of the oscillating lift force. It can be seen from the figure that the wall-induced lift and the vortex-induced lift appear to be in the same order of magnitude at $e/D = 0.3$. With decreasing gap, however, the wall-induced lift seem to increase quite substantially. The figure also demonstrate that for gap ratios > 0.3, both the wall-induced lift and the vortex-induced lift may be present, giving the cylinder a steady lift $\neq 0$ which is oscillating due to the vortex shedding. [Sumer and Fredsøe, 1997]

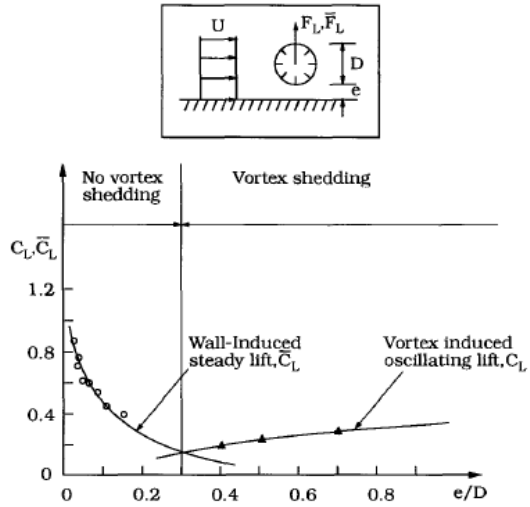

Figure 2.9: Force coefficients of the mean lift force and the oscillating lift force on a cylinder as a function of the gap ratio. The oscillating lift coefficient is based on the amplitude of lift. Figure found in [Sumer and Fredsøe, 1997]

2.6 Correlation length

As mentioned in Section 2.1, the vortex shedding in the wake takes place in cells in the spanwise direction for $Re > 200$. Shedding might not occur uniformly along the length of the cylinder. A consequence of this is that the maximum force on the cylinder over its total length may be smaller than the force acting on the cylinder over the length of a single cell. The averaged length of one cell is called the correlation length, L, and may be decided from experiments. For a smooth cylinder the correlation length changes with Re. According to Sumer and Fredsøe (1997) is the correlation length for $150 < Re < 10^5$ found to be $(2-3)D$. The correlation length may also be affected by e.g turbulence in incoming flow and if the cylinder is oscillated in the crossflow direction.

Chapter 3

Numerical method: Large Eddy Simulation

According to Ferziger and Peric (1997), can the conservation of mass for an incompressible and isothermal flow be written

$$\text{div } \vec{v} = 0 \tag{3.1}$$

The momentum conservation is given by

$$\frac{\partial u_i}{\partial t} + \text{div } (u_i \vec{v}) = \text{div } (\mu \text{ grad } u_i) - \frac{1}{\rho}\text{div } (p\vec{i}_i) + b_i \tag{3.2}$$

Turbulent flows contain a large range of length and time scales. The length scales of eddies which might be found in the flow are illustrated schematically in Figure 3.1. The right side of the figure shows velocity component at a fixed point in the flow and illustrate the time dependence.

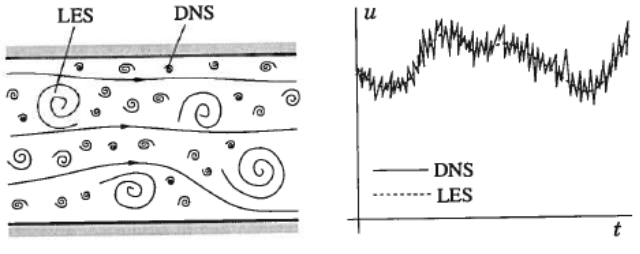

Figure 3.1: Schematic representation of turbulent motion (left) and the time dependence of a velocity component (right) from [Ferziger and Peric 1997]

In turbulence, the large scale motions are much more energetic that the small scales. Their strength make the large scale eddies more effective transporters of the conserved properties than the small ones. Therefore, a simulation which treats the large eddies more exactly than the small scale ones is logical, and Large Eddy Simulation (LES) is such an approach. LES are three dimensional, time dependant and expensive, but much less costly than direct numerical simulations (DNS) When the Reynolds number is too high for DNS or the geometry is too complex, LES is preferred.

In order to use LES, the velocity field must only contain the large scale components of the total field. This is done by filtering. The large scale field which is to be simulated is essentially a local average of the complete field. The principles for filtering are described by Ferziger and Peric (1997).

The filter is associated with a length scale Δ. In a rough sense, the eddies of size larger than Δ are large eddies while those smaller than Δ are small eddies. The small ones will need to be modelled. The filtered Navier-Stokes equations for constant density are very similar to the Reynolds-Averaged Navier-Stokes equations:

$$\frac{\partial(\rho\overline{u}_i)}{\partial t} + \frac{\partial(\rho\overline{u_i u_j})}{\partial x_j} = -\frac{\partial \overline{p}}{\partial x_i} + \frac{\partial}{\partial x_j}\left[\mu\left(\frac{\partial \overline{u}_i}{\partial x_j} + \frac{\partial \overline{u}_j}{\partial x_i}\right)\right] \tag{3.3}$$

Because the continuity equation is linear, it does not change significantly:

$$\frac{\partial(\rho\overline{u}_i)}{\partial x_i} = 0 \tag{3.4}$$

Since $\overline{u_i u_j} \neq \overline{u_i}\ \overline{u_j}$ and the left side of the inequality is not easily computed, a modelling approximation for the difference between the two sides of the inequality

$$\tau_{ij}^s = -\rho(\overline{u_i u_j} - \overline{u}_i \overline{u}_j) \tag{3.5}$$

In the context of LES, τ_{ij}^s is called the *subgrid scale Reynolds stress* (SGS stress). The name *stress* comes from the way it is treated, rather than its physical nature. In fact, it is the large scale momentum flux caused by the action of the small or unresolved scales. The name *subgrid* can be confusing. The width of the filter Δ does not necassary have anything to do with the grid size h, other than that $\Delta > h$ The models which are used to approximate the SGS stress are called *subgrid scale (SGS) models*.

The subgrid scale Reynolds stress is a local average of the small scale field. Therefore, models should be based on the local velocity field or the perhaps on the past history of the local fluid. [Ferziger and Peric 1997]

3.1 The Smagorinsky Subgrid Scale Model

The most commonly SGS model is the Smagorinsky subgrid scale model. This is an eddy viscosity model, meaning that it is based on the notion that the effects of the SGS Reynolds stress are increased transport and dissipation. Since increased transport and dissipation are effects of viscosity in laminar flows, then according to Ferziger and Peric (1997) can a reasonable model might be:

$$\tau_{ij}^s - \frac{1}{3}\tau_{kk}^s\delta_{ij} = \mu_t\left(\frac{\partial\overline{u}_i}{\partial x_j} + \frac{\partial\overline{u}_j}{\partial x_i}\right) = 2\mu_t\overline{S}_{ij} \tag{3.6}$$

where μ_t is the eddy viscosity.

The subgrid scale viscosity is given by

$$\mu_t = C_S^2\rho\Delta^2|\overline{S}| \tag{3.7}$$

where C_S is the model parameter, Δ is the filter length scale, $|\overline{S}| = (\overline{S}_{ij}\overline{S}_{ij})^{1/2}$. For all analyses, C_S has been set to 0.1 in this thesis. This is based on both recommendations from CD-adapco (2013) and Prsic et al. (2012).

One should note that the value for C_S should be reduced close to surfaces (i.e the cylinder wall). The van Driest damping function provides this. This was applied by Breuer (1998a) among others. However, it can cause the computational time to increase for parallel simulations. [Abrahamsen-Prsic, 2013; CD-adapco, 2013] For Prsic et al. (2012), the results were satisfying without damping of the Smagorinsky SGS model. After conversations with Abrahamsen-Prsic (2013) it was decided not to apply the van Driest damping function.

3.2 Solver

The implicit unsteady solver is the only available time solver for constant-density transient analysis in STAR-CCM+, and has thus been applied. A 2nd order temporal discreatization scheme has been applied. For flow model, one can choose between coupled and segregated flow. The segregated solver is faster and uses less memory for incompressible flow according to CD-adapco (2013); Support, CD-adapco - Star-CCM+ (2013). The segregated flow model solves the flow equations (one for each velocity component and one for pressure) in an uncoupled manner. The momentum and continuity equations are linked with a predictor-corrector approach. More information about the solver can be found in [CD-adapco, 2013].

3.3 Differencing scheme

The applied convection scheme is a bounded central differencing-scheme. The bounded central-differencing scheme will turn into a first-order upwind scheme when the convection boundedness criterion is not satisfied. Beyond that it is, like the central-differencing scheme, a second order accurate scheme. Overall, the bounded central-differencing scheme provides a good compromise between accuracy and robustness, and it is the recommended scheme for LES by CD-adapco (2013) Breuer (1998a) concluded that for LES central differencing schemes of second- or forth-order are well suited. On the other hand, one can note that upwind schemes not was recommended by Breuer (1998a). More information about the differencing scheme can be found in [CD-adapco, 2013].

3.4 Time step and number of iterations

During the analysis, the CFL number was observed. The CFL number is given $\text{CFL} = \frac{u\Delta t}{\Delta x}$ and should be low for LES. For all analyses, the chosen time step was $\Delta t = 0.0002$ s, which gives a non-dimensional time step of $\Delta t \cdot D/U_c = 5.13 \cdot 10^{-5}$. This was decided after conversations with Abrahamsen-Prsic (2013). The number of inner iterations per time step was set to 16 for the analyses. The number of inner iterations per time step was attempted optimized as a compromise between accuracy and computational time, see Chapter 6.

Chapter 4

Preprocessing

All preprocessing are performed using STAR-CCM+. The general workflow in this software is to prepare the geometry, define the simulation topology, generate the mesh, define the physics, prepare for analysis, run the analysis and analyse the results. Thingbø (2012) described the creation of computational domain, regions and boundaries. In this thesis, only the most relevant information for the two cases are given.

4.1 Structured meshing in STAR-CCM+

Why discretization is needed, general information about finite volume discretization and mesh generation in STAR-CCM+ is described by Thingbø (2012).

For all three simulations in this thesis, structured mesh have been applied. In STAR-CCM+ this is available by using the directed mesher for CAD geometries. The directed mesher operates by sweeping the a surface mesh from the surface of the CAD geometry through its volume. For such simple geometries as in this thesis the directed mesher is easy to use and gives a great degree of control for volume mesh generation. The mesh created will be hexahedral. A source surface and a target surface in defined for the CAD geometry, i.e the computational domain. A source mesh is created on the source surface. The volume between the source surface and the target surface will then be sweeped with a given volume distribution of the created two-dimensional source mesh.

The source mesh is in this thesis generated in a XY-plane, at Z = -2D. The target surface is also in a XY-plane, at Z = 2D. At the source mesh, patches were created. Within the patches, one can create quad cells. When this is done for the entire source surface, the source mesh is finished and the volume distribution can be defined. The three-dimensional volume mesh is then ready to be generated.

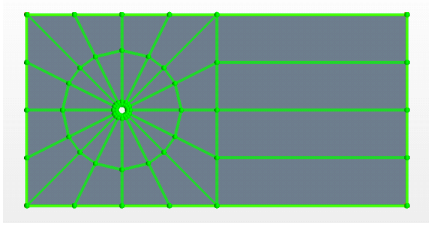

(a) An example of a patch topology used in Case 1

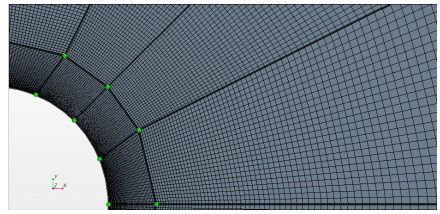

(b) A part of the patch mesh for Case 1

Figure 4.1: Illustration of a patch topology and a patch mesh generated in STAR-CCM+ for Case 1

4.1.1 Mesh diagnostics

In order to check whether the mesh is good, a full mesh diagnostics report were ran for all meshes generated in this thesis. The mesh diagnostics report were applied to check the mesh for

- Mesh validity
- Face validity
- Volume change statistics
- Maximum interior skewness angle
- Maximum boundary skewness angle

The mesh validity checks for unclosed cells, invalid cells or vertex references, zero face area, and zero or negative volume cells. The face validity is an area-weighted measure of the correctness of the face normals relative to their attached cell centroid. The volume change statistics describes the maximum and minimum ration of the volume of a cell to that of its largest neighbours. Cells with a volume change of 10^{-5} or below should be investigated. [CD-adapco 2013] Both the mesh validity, the face validity and the volume change statistics were fine for all meshes.

A skewness angle of 90 degrees or more, which can occur in concave cells, are problematic in STAR-CCM+. Due to this, it is not recommended to have any skewness angle greater than 85 degrees. For all analyses the maximum skewness angle was kept below 50 degrees.

The aspect ratio was also investigated for the different meshes. The cells in the mesh are preferred to be regular polygonal cells, not highly stretched. This can be investigated by using a scalar scene and the cell aspect ratio field function. In addition, the bad cell indicator field function was applied in all meshes to check for cells that are considered bad, none were found. [CD-adapco, 2013]

4.2 Applied boundary conditions

The boundaries for the computational domain must be given physical properties. This section describes the different types of boundaries chosen in STAR-CCM+. Were the different types are applied are given in Chapter 7 and Chapter 8. The different cases are described in these chapters. More information regarding the boundary conditions can be found in [CD-adapco, 2013].

Velocity Inlet

In STAR-CCM+ the boundary condition *Velocity Inlet*, i.e. the inlet face velocity vector, is specified directly. The boundary face pressure is extrapolated from the adjacent cell using reconstruction gradients.

Pressure Outlet

Pressure Outlet specifies the pressure on the outlet boundary to be equal to zero. At the pressure outlet the boundary face velocity is extrapolated from the interior using reconstruction gradients.

Symmetry Plane

In a *Symmetry Plane*, the shear stress is set to zero in STAR-CCM+. As for the *Pressure Outlet*, the face value of the velocity is extrapolated from the parallel component of the velocity in the adjacent cell. The boundary face pressure is calculated the same way.

Wall

By using this boundary condition, the tangential velocity at the boundary is set to zero. The boundary layer face pressure is extrapolated from the adjacent cells using reconstruction gradient. There will not be any velocities through a boundary defined as a wall.

Periodic Interface

Two boundaries can be defined as a periodic interface. The boundaries are then physically separated in space but can be mapped from one to the other by a constant translation. The periodic boundary represents a cyclic repeat of information across the boundaries, so fluxes that cross one boundary are transformed and applied to the other. The mesh on the two boundaries defined with a periodic interface must be conformal, i.e the mesh must be equal on the boundaries.

4.3 Applied physical models in STAR-CCM+

In STAR-CCM+, the *physics module* defines how a physical phenomenon in a continuum is represented. The physics modules defines the primary variables of the simulation (in this case pressure and velocity) and what mathematical formulation which is used to find the solution. A combination of models is necessary to for the complete definition of a physics continuum.

In STAR-CCM+ the physics models and methods are selected using a *physics continuum*. In all analyses in this thesis, the following physics models have been used:

- Space: Three Dimensional
- Time: Implicit Unsteady
- Material: Liquid
- Flow: Segregated Flow
- Equation of State: Constant Density
- Viscous Regime: Turbulent
- Turbulence: Large Eddy Simulations
- Subgrid Scale Turbulence: Smagorinsky Subgrid Scale
- LES Wall Treatment: Low y^+ Wall Treatment

Chapter 5

Postprocessing

In STAR-CCM+ one can create different types of plots and scenes. The plots and scenes are set up before running the simulation, and can be analysed when the stopping criteria is satisfied and the simulation is finished. One can also look at the plots and scenes while the simulation is running, which can be informing in the beginning. In this thesis, the plots and scenes have been used also to evaluate when the flow is considered to be fully developed. How reports, monitors, plots, graphic scenes and animations are created in STAR-CCM+ are explained in [Thingbø, 2012].

In this thesis the following scenes have been used to obtain the graphical results

- Scalar scene for velocity component u
- Scalar scene for velocity component v
- Scalar scene for the pressure contour lines
- Scalar scene for the velocity contour lines
- Scalar scene for the vorticity contour lines
- Scalar scene for the convective courant number
- Scalar scene for the δ^+-value at the cylinder wall and the Y^+-value at the seabed
- Scalar scene of isosurfaces for λ_2.

Note that only the scalar scene of isosurfaces for λ_2 is presented in this report.

5.1 Averaging in space and time

In this thesis the statistical results are given for velocity components u, v and w. In addition the pressure coefficient C_p is calculated. To obtain the spanwise average the results are found for 15 lines in the spanwise direction, and then the average of these lines are found. This is demonstrated for in Figure 5.1 and in Figure 5.2. In Figure 5.1, the 15 lines applied to find the spanwise average for some of the velocity profiles in the wake are shown.

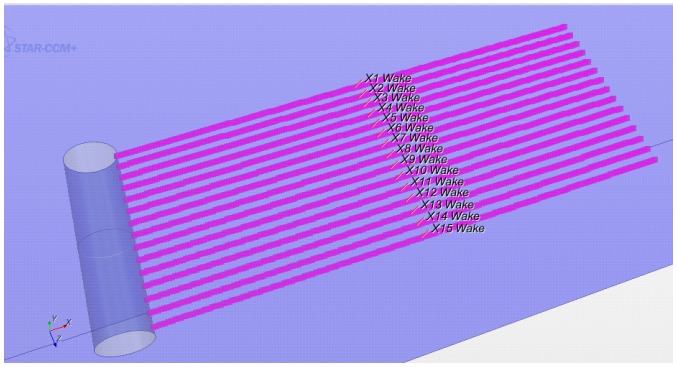

Figure 5.1: Example of lines in the wake of the cylinder applied for spacial averaging

In Figure 5.2 the 15 lines applied to find the spanwise average for C_p are shown.

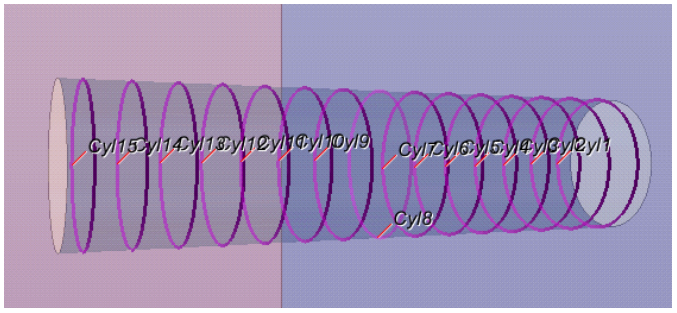

Figure 5.2: Example of lines on the cylinder wall applied for spacial averaging of C_p

In addition to the spacial averaging, it is sufficient to average over time, in order to collect statistics from the analysis. This was done by using *field mean*-monitors in STAR-CCM+. When the simulations have finished running, it is then possible to plot these results or use the averaged data in graphical scenes. In the analyses the following space- and time-averaged plots have been used.

- Plot of the time-averaged pressure coefficient for the cylinder wall
- Plots of space- and time averaged velocity profiles

In addition, plots for the drag coefficient and the lift coefficient for the cylinder have been made, and the time averaged C_D and $C_{L,rms}$ are found.

5.1.1 MATLAB

All plots created in STAR-CCM+ was tabulated and exported. MATLAB was applied for further analysis, and here the spacial average of the lines distributed in Z-direction, mean C_D, $C_{L,rms}$ and St were calculated. MATLAB was also useful for creating shared plots for the different simulations.

Chapter 6

Computational Time

In this thesis, one of the most challenging problems was to decrease the computational time of the analyses, so that they were finished before the thesis deadline. Thus, many different strategies was tested. This chapter describes the efforts to reduce the computational time. LES simulations require a sufficiently small time step to resolve the turbulent time scales. Also, LES require a good mesh with $\delta^+ \leq 1$. The CFL number should be low. This results in a large amount of cells and many time steps.

6.1 The supercomputer Vilje

In order to apply LES for the three-dimensional analyses in this thesis, a large amount of computational resources were required. Due to this, the analyses were executed on the supercomputer Vilje. In order to run analyses, the jobs are submitted to a queue.

Some node details for Vilje:

- Number of nodes: 1404
- Processors per node: 2 eight-core processors
- Processor speed: 2.6 GHz
- L3 Cache: 20 MB / 8 cores
- Memory: 20 GB per core
- Operational system: SUSE Linux Enterprice Server 11
- Scheduler: PBS
- Compilers: Intel and GNU C and Fortran

- MPI library: SGI MPT

The details regarding Vilje is given by NTNU HPC GROUP (2012).

At first, it was assumed that 4 node was enough. After some testing, it could be seen that this would result in a computational time for approximately 31 000 days for *one* simulation. The number of nodes was increased, and the final number of selected nodes was 36. A simulation using 36 nodes, 72 processors and 576 cores was assumed to give a computational time of approximately 20 days. The chosen number of nodes were based on both testing and conversations with Abrahamsen-Prsic (2013).

6.2 Time step, residuals and iterations per time step

Support, CD-adapco - Star-CCM+ (2013) recommended a time step in the range between 10^{-5} and 10^{-6} seconds. Prsic et al. (2012) obtained satisfying results with a time step of $2 \cdot 10^{-4}$ seconds. This was therefore chosen timestep, in order to save some computational time.

In STAR-CCM+, it is possible to set different stopping criteria for the iterations. One of them is to set a maximum value for the residual of conservation of mass and conservation of momentum in X-, Y- and Z-direction. For these analyses the initial strategy was to set the maximum limit for the residuals to $1 \cdot 10^{-7}$. However, this caused too many iterations per time step, and thus too long computational time. The maximum limit was tried increased to both $1 \cdot 10^{-6}$ and $5 \cdot 10^{-6}$. Still, the computational time was too long, because for some time steps far too many iterations were needed to reach the maximum limit for the residuals. Also, the number of iteration needed for the different time steps varied and the thus computational time was unpredictable. Due to these problems, it was decided to not use the maximum limit for the residuals as a stopping criteria for iterations. Instead a constant number for iterations per time step was set. This was changed for the different time intervals of the simulation. Table 6.1 shows the number of inner iterations for the different time intervals for each simulation.

Table 6.1: Number of iterations for different time intervals

	Physical Time Interval		
	0 - 1 [s]	**1 - 35** [s]	**35 - 100** [s]
Iterations per timestep: Case 1	200	12	16
Iterations per timestep: Case 2a	200	12	16
Iterations per timestep: Case 2b	200	12	16

According to Support, CD-adapco - Star-CCM+ (2013), one can assume that the time step has converged if the residuals drops 2-3 order of magnitude within the

iterations. This has been monitored during the simulations for both the continuity, X-momentum, Y-momentum and Z-momentum. However, one should note that the residuals did not drop to a value 10^{-7}. A larger number of inner iterations could have given better results, but if this were utilized, the results would might not have been ready before the thesis deadline.

6.3 Elements in the spanwise direction

The final adjustment for reducing the computational time was to reduce the number of elements in the spanwise direction. The number was reduced from 60 elements to 42 elements, and hence the total number of cells in the domains was reduced. The effect of this is fewer equations to be solved for each iteration, and hence shorter computational time.

6.4 Mesh convergence

For Case 2a, a mesh convergence study was performed, see Chapter 8. The strategy which made this possible was to first run one simulation until steady state solution. Then two copies with the obtained solution was saved, and remeshed. The obtained solution was interpolated by STAR-CCM+ to the new grid for the actual time step. The two new simulations continued to run further for $10 \cdot T_V$ before the collection of data for the statistics began.

With the final set-up the computational time for the two different cases was approximately 18 days for Case 1 and 21 days for Case 2.

Chapter 7

Case 1

7.1 Physical Parameters

Case 1 describes a circular cylinder in infinite fluid, subjected to a uniform flow. The case is three-dimensional and the Reynolds number is set to 3900, i.e the flow regime is subcritical and the boundary layer over the cylinder remains laminar.

In the following analysis, the diameter, D, is set to 0.1 m. In order to obtain Reynolds number 3900, the parameters U_c, ρ and μ were scaled. Their values can be seen in Table 7.1.

Table 7.1: Physical parameters for Case 1

Physical parameters for Case 1				
U_c [m/s]	D [m]	ρ [kg/m^3]	μ [kg/ms]	Re [-]
0.39	0.1	1	10^{-5}	3900

7.2 Computational Domain

When choosing a computational domain for Case 1, it is important that the fluid flow around the cylinder does not 'feel' any of the boundaries. In other words, the boundaries of the computational domain shall not affect the fluid flow in any way. The choice of domain size was based on established standards for the benchmark case and recommendations from Abrahamsen-Prsic (2013).

The chosen domain size (X, Y, Z) is 32D · 16D · 4D. The centre of the cylinder is placed 8D downstream of the inlet boundary, 8D from the top and bottom boundary and 24D from the outlet boundary. The domain is illustrated in Figure 7.1.

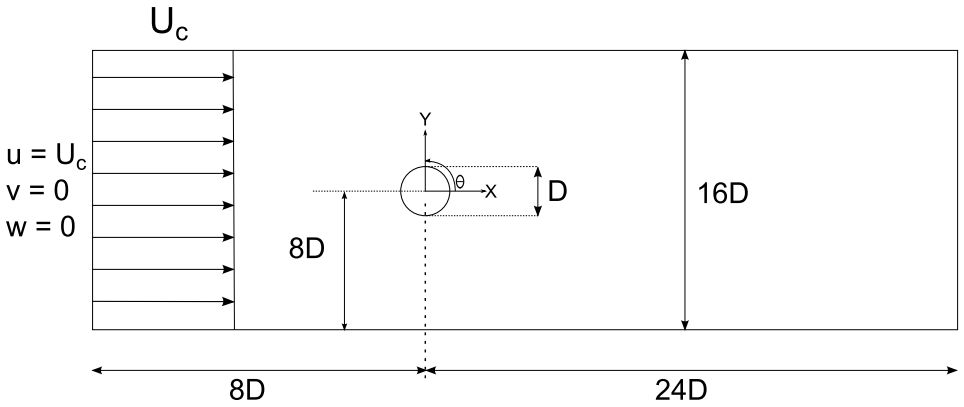

Figure 7.1: The set-up for Case 1 in the XY-plane

Parnaudeau et al. (2008) and Tremblay et al. (2000) used a domain size (X, Y) of 20D · 20D, where the cylinder was placed 5D from the inlet boundary. The spanwise extent was πD. Franke and Frank (2002) used a larger domain where the size (X, Y, Z) was 30D · 20D · πD. The centre of the cylinder was placed 10D downstream of the inlet boundary. Wissink and Rodi (2008a) used a computational domain of size (X, Y, Z) 25D · 20D · 4D. Li (2011) used a bit smaller domain of (X, Y, Z) 27D · 9D · 2.3D where the cylinder centre was placed 4.5D downstream of the inlet boundary. Breuer (1998a,b) used a circular domain instead of a rectangular. The radius og the domain in the XY-plane was 15D and the spanwise extent was πD. Compared to the mentioned studies, the chosen computational domain should be sufficiently large.

7.3 Mesh

The number of elements i X- and Y-direction is based on the mesh convergence study by Prsic et al. (2012). Here, the mesh convergence study was performed for 5 million, 8 million and 11 million cells. For all three cases, 150 elements were used in the spanwise (Z) direction. The number of circumferential elements was varied from 340 to 480. The conclusion was that the finest grid with 11 million cells was a sufficient grid resolution. The mesh for Case 1 is in addition to this, based on conversations and recommendations from Abrahamsen-Prsic (2013).

The mesh for Case 1 is divided into four zones. Zone 1 is a a small fairly O-shaped zone closes to the cylinder. Zone 2 is the zone outside of Zone 1, and is also quite O-shaped. Zone 3 is between Zone 2 and the boundaries of the computational domain, its outer region is square-shaped. Zone 4 is in the far wake. All cells are fairly stretched away from the cylinder. The zones can be seen in Figure 7.2

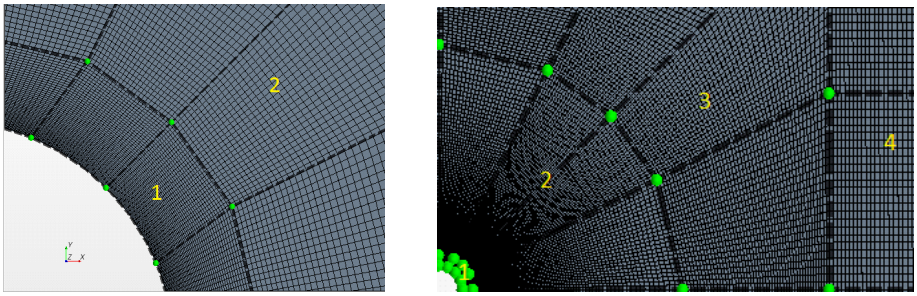

(a) Zone 1 and Zone 2 **(b)** Zone 2, Zone 3, and Zone 4

Figure 7.2: Parts of Zone 2, Zone 3 and Zone 4. Zone 1 is difficult to see because of its small size.

For Case 1, the number of elements in the radial direction was 200 to the outer boundary of zone 3, and the number of elements in the circumferential direction around the cylinder was 400. The number of elements (X×Y) in the far wake was 100×100, and these were fairly stretched away from the cylinder. The total number of elements in the XY-plane was 90 000. However, due to the computational time, the number of elements in the spanwise could not be set to 150. In Case 1, the spanwise resolution was set to 42 elements. This was based on similar analyses. Parnaudeau et al. (2008) used a spanwise resolution of 48 elements. Breuer (1998a,b) used a number of elements equal to 32 in Z-direction for most of the analyses. Franke and Frank (2002) used a number of 33 grid points in the spanwise direction. Li (2011) did a mesh convergence study and concluded that both 16, 32 and 48 elements in the spanwise direction gave results in good agreement with experimental data. Wissink and Rodi (2008a) used a spanwise resolution of as many as 512 elements. Hence, the chosen number of elements in the spanwise direction is within the range of the previous similar performed analyses, but at the lower side of the scale.

For the analysis, the height of the elements closest to the cylinder wall in radial direction is kept equal to $\delta = 0.0002$ m. This ensures a value for δ^+ below 1 and was also used by Prsic et al. (2012). The cells around the cylinder were prismatic.

δ^+ is given as

$$\delta^+ = \frac{u_* \delta}{\nu} \tag{7.1}$$

Where δ is the element height in radial direction and u_* is the friction velocity at the nearest wall. It was assumed that $u_* < U_c$.

A summary of the mesh and main parameters for Case 1 is given in Table 7.2.

Table 7.2: Numerical set-up for Case 1

	Domain (·D)	**Elements [million]**	**Num. elem. spanwise**	**Num. elem. circumf.**	U_c **[m/s]**	$\Delta t \cdot D/U_c$ **[-]**
Case 1	32·16·4	3.78	42	400	0.39	$5.13 \cdot 10^{-5}$

7.4 Initial Conditions and Boundary Conditions

For this analysis, the initial condition was set for the velocity of the uniform current, u = U_c, $v = w = 0$. U_c was set to 0.39 m/s. The type of boundary condition and values for the physical parameters which have been used are

- At the inlet: Velocity Inlet. Uniform constant inlet velocity: $U_c = 0.39$ m/s
- At the outlet: Pressure outlet.
- Top and bottom boundary: Symmetry plane
- The two sides which defines the spanwise extent: Periodic interface
- Cylinder wall: Wall

Chapter 8

Case 2

Case 2 describes a circular cylinder close to the seabed. Flow around a cylinder close to a wall depends on the shape of the incoming boundary layer profile. Due to this, Case 2 is divided into to subcases: Case 2a and Case 2b. The difference between the cases is the velocity profile at the inlet boundary. A mesh convergence study was performed for Case 2a.

As for Case 1, the Case 2 is three-dimensional and the Reynolds number based on the flow at the cylinder centre is set to 3900. The case is chosen with this Reynolds number so that the physics can be compared to Case 1. The gap, e, between the cylinder wall and the seabed is set to $0.2 \cdot D$.

8.1 Case 2a

8.1.1 Physical Parameters

In Case 2a the diameter, D, is set to 0.1 m. The Reynolds number was kept equal to 3900. The parameters, U_c, ρ and μ were scaled in order to obtain the Reynolds number. The parameters are given in Table 8.1.

Table 8.1: Physical parameters for Case 2a

Physical parameters for Case 2a				
U_c [m/s]	D [m]	ρ [kg/m^3]	μ [kg/ms]	Re [-]
0.39	0.1	1	10^{-5}	3900

8.1.2 Computational Domain

The computational domain is illustrated in Figure 8.1. Ong et al. (2008, 2010) used a two-dimensional domain of (X, Y) 30D · 10D. The cylinder was placed 10D downstream of the inlet boundary. Sarkar and Sarkar (2010) applied a domain of (X, Y, Z) 30D · 8.5D · 3D, where the cylinder was placed 5D from the inlet boundary. Lei et al. (2000) applied a two-dimensional domain of (X, Y) 26D · 10D + e. The origin of the cylinder was placed 16D from the inlet boundary. The size of the domain for Case 2 was decided after conversations with Abrahamsen-Prsic (2013), and should be sufficiently large. The extension of the domain is set to be (X, Y, Z) 40D · 10D · 4D and the cylinder is placed 10D downstream of the inlet boundary, see Figure 8.1.

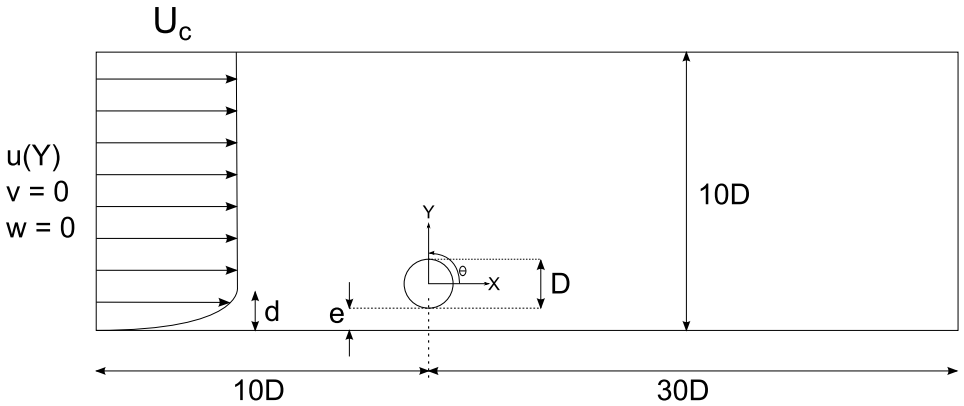

Figure 8.1: The set-up for Case 2a in the XY-plane

8.1.3 Mesh

For Case 2a, a mesh convergence study was performed. The mesh distribution was kept constant in Z-direction. According to Abrahamsen-Prsic et al. (2013), the mesh for this case was not so sensitive in Z-direction, and thus the distribution of elements in the circumferential and radial direction was varied. The number of cells the spanwise direction was 42 for all analyses in Case 2a. Thee different meshes was investigated, and they are summarized in Table 8.2.

Table 8.2: Numerical set-up for Case 2a

	Domain (·D)	**Elem. [million]**	**Num. elem. spanwise**	**Num. elem. circumf.**	U_c **[m/s]**	$\Delta t \cdot D/U_c$ **[-]**
Case 2a_1	40·10·4	5866140	42	526	0.39	$5.13 \cdot 10^{-5}$
Case 2a_2	40·10·4	4268880	42	456	0.39	$5.13 \cdot 10^{-5}$
Case 2a_3	40·10·4	3295740	42	388	0.39	$5.13 \cdot 10^{-5}$

The mesh for Case 2 was more challenging than for Case 1. Is was attempted to

create a mesh with good transitions. The mesh for Case 2 is divided into six zones. Zone 1 is a a small fairly O-shaped zone closes to the cylinder. Zone 2 is the zone outside of Zone 1, and is also quite O-shaped. Zone 3 outside of Zone 2, and Zone 4 is outside of Zone 3. Zone 5 is in the far wake. Zone 6 is the zone above the seabed which ensures prismatic cells in the boundary layer. All cells are fairly stretched away from the cylinder. The zones can be seen in Figure 8.2.

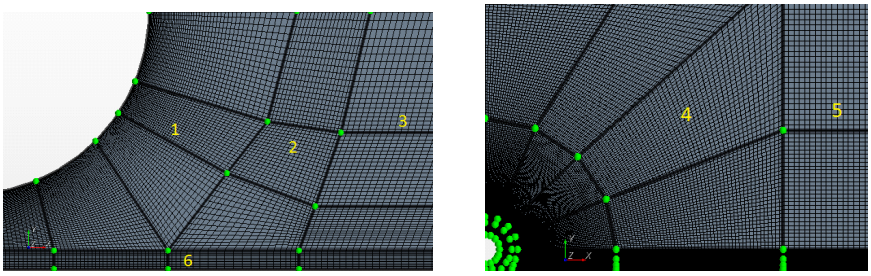

(a) Zone 1, 2, 3 and 6 **(b)** Parts of Zone 4 and Zone 5

Figure 8.2: The different zones for the mesh in Case 2

As for Case 1, the height of the elements closest to the cylinder wall in radial direction is kept equal to $\delta = 0.0002$ m. This ensures a value for δ^+ below 1. This value is kept constant in the mesh convergence study. The height of the element closest to the seabed in Y-direction, is kept equal to $Y = 0.0003$ m. This ensures a Y^+-value below 1, and is used for both Case 2a_1, Case 2a_2 and Case 2a_3. Both cells around the cylinder wall and along the seabed are prismatic.

8.1.4 Initial Conditions and Boundary Conditions

For Case 2a, the initial condition was set for $u = u(Y)$ and $v = w = 0$. The different boundary conditions are explained in section 4.2. The type of boundary condition and values for the physical parameters which have been used are

- At the inlet: Velocity Inlet. $u(Y)$ given in Eq 8.1, $v = w = 0$
- At the outlet: Pressure outlet.
- Top boundary: Symmetry plane
- Seabed: Wall
- The two sides which defines the spanwise extent: Periodic interface
- Cylinder wall: Wall

The velocity profile $u(y)$ is equal to the one used by Ong et al. (2008). The chosen logarithmic profile should simulate a naturally developed boundary layer profile

near a flat, rigid seabed. The flow is allowed to develop $x/D = 10$ before it reaches the cylinder and is given by Eq 8.1.

$$u(Y) = \min\left\{ \frac{u_*}{\kappa} \ln\left(\frac{Y}{z_w}\right), U_c \right\} \tag{8.1}$$

Here the friction velocity is evaluated as $u_* = \frac{\kappa U_c}{\ln(\delta/z_w)}$. κ is the von Karman constant and is equal to 0.41. z_w is the roughness for the seabed and is set to be $1 \cdot 10^{-6}$. This value is according to Ong et al. (2008) preferred due to enchanted numerical stability, but leads to almost the same result as a smooth logarithmic wall function. U_c is the free-stream velocity and is set to 0.39 m/s to give $Re = 3900$. δ is the boundary layer thickness and $\delta/D = 0.48$. With a gap $e = 0.2D$, the cylinder is partly submerged in the boundary layer, and the gap-to-boundary-layer-thickness ratio, e/δ, is equal to 0.42.

8.2 Case 2b

8.2.1 Physical parameters

The case consists of a circular cylinder close to the seabed. The case is three-dimensional and the Reynolds is equal to 3900. Like Case 2a, Case 2b is chosen with this Reynolds number so that the physics can be compared to Case 1. The gap, e, between the cylinder wall and the seabed is also here set to $0.2 \cdot D$. The physical parameters are summarized in Table 8.3.

Table 8.3: Physical parameters for Case 2b

Physical parameters for Case 2b				
U_c [m/s]	D [m]	ρ [kg/m^3]	μ [kg/ms]	Re [-]
0.39	0.1	1	10^{-5}	3900

All physical parameters are equal to the ones in Case 2a, except of the velocity profile at the inlet boundary. In Case 2b the flow at the inlet is steady and uniform, and the velocity in X-direction, u, is equal to $U_c = 0.39$ m/s.

8.2.2 Computational domain and mesh

The computational domain for Case 2b is the equal to the domain in Case 2a. The mesh is the same as the one applied in Case 2a_2, see Table 8.2. The case is illustrated in Figure 8.3.

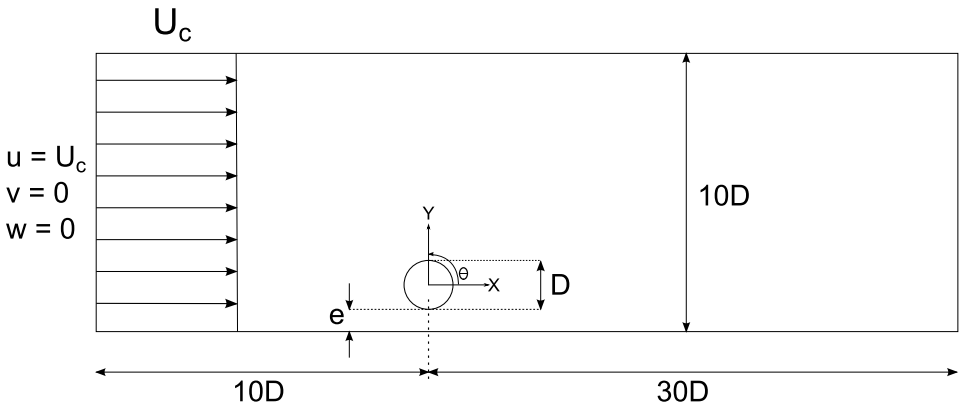

Figure 8.3: The set-up for Case 2b in the XY-plane

8.2.3 Initial Conditions and Boundary Conditions

For Case 2b, the initial condition was set for $u = U_c$ and $v = w = 0$. The different boundary conditions are explained in section 4.2. The type of boundary condition and values for the physical parameters which have been used are

- At the inlet: Velocity Inlet. $u = 0.39$ m/s, $v = w = 0$
- At the outlet: Pressure outlet.
- Top boundary: Symmetry plane
- Seabed: Wall
- The two sides which defines the spanwise extent: Periodic interface
- Cylinder wall: Wall

Chapter 9

Results and discussion

All results in this thesis are time-averaged for approximately 50 vortex shedding-periods, and the statistics were averaged in the spanwise direction as well. The averaging operator is denoted $\langle\rangle$.

9.1 Case 1

Although the geometric is simple, the circular shape of the cylinder is a challenge for numerical studies. No sharp edges determine the points of separation. The location is purely fixed by the flow regime or the upstream conditions. Due to this, numerical predictions of the turbulence statistics in the near region are very sensitive and can lead to nonconformities.

Lysenko et al. (2012) concluded that the available research reveals the existence of the flow bifurcation for this benchmark case (U-shape and V-shape). Both the U-shape and the V-shape was obtained by Lysenko et al. (2012). Wissink and Rodi (2008b) concluded that an U-shape solution is more likely by applying an extremely high-resolved mesh and DNS. However, both flows have been identified experimentally; U-shape by Parnaudeau et al. (2008) and V-shape by Lourenco and Shih (1993) (according to Lysenko et al. (2012)). Prsic et al. (2012) obtained the V-shape and Parnaudeau et al. (2008) obtained the U-shape in the numerical LES simulations.

9.1.1 Instantaneous flow field and mean flow field parameters

Figure 9.1 shows the time histories for the lift and drag coefficients for a period of approximately 50 vortex shedding periods. According to Lysenko et al. (2012), the

irregularity in forces may be explained by irregular three-dimensional break up of vortices.

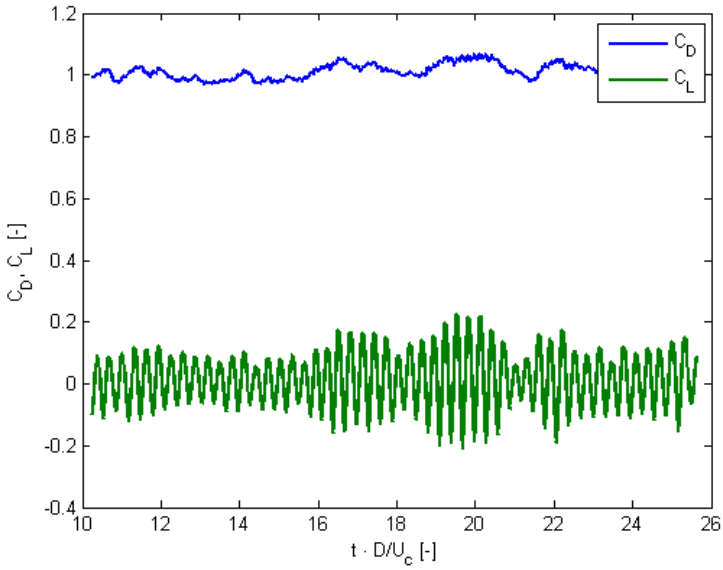

Figure 9.1: Time history of the lift C_L and the drag C_D coefficients for $\approx$ 50 vortex shedding cycles

To get a better understanding of the physics in Case 1, three snapshots of the λ_2 eigenvalue equal to -0.004 are shown in Figure 9.2. According to CD-adapco (2013), values of $\lambda_2 < 0$ can be interpreted as vortex regions.

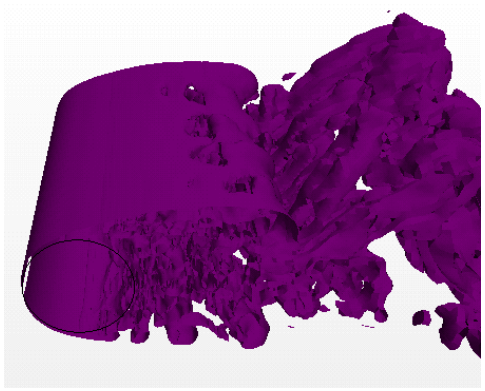

(a) $\lambda_2 = -0.004$ at $t = 100.00$ s

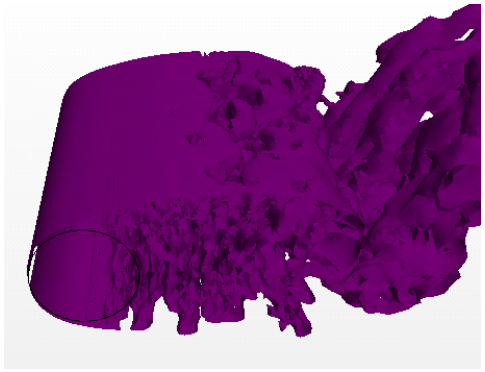

(b) $\lambda_2 = -0.004$ at $t = 100.49$ s

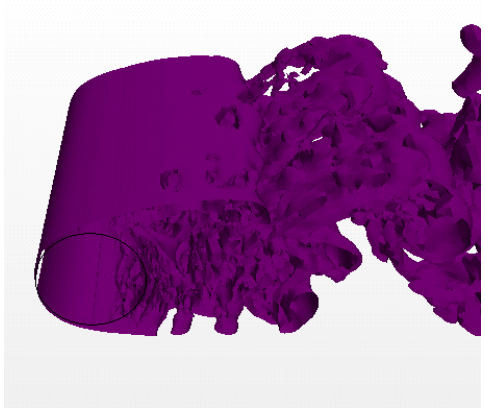

(c) $\lambda_2 = -0.004$ at $t = 100.98$ s

Figure 9.2: Snapshots showing isosurface of $\lambda_2 = -0.004$ in the near wake

From Figure 9.2, the three dimensional effects in the flow can be observed. The free

shear layers is mainly two dimensional. Just upstream of where the shear layers roll up, a spanwise variation of the free shear layers is can be seen. This position corresponds to the transition from 2D to 3D flow. The snapshots are taken with a difference in time, $\Delta t \approx 0.5s$. In Figure 9.2a, the vortex is shed from the lower side of the cylinder. In Figure 9.2b the vortex is soon to shed from the upper side of the cylinder. This is validated with the variations in the lift force. Note that these snap-shots do not give any validation of whether the simulation is of good quality or not. [Abrahamsen-Prsic, 2013]

Results are analysed through space- and time-averaged standard hydrodynamic parameters of drag and lift coefficients. The results are compared to what was found by Lysenko et al. (2012) with the dynamic k-equation eddy viscosity SGS model (subsequently called TKE), Breuer (1998a), (Franke and Frank, 2002), Ong and Wallace (1996), Parnaudeau et al. (2008) and Prsic et al. (2012) in Table 9.1

Table 9.1: Mean flow parameters for Case 1 and previously published results

Case	$\langle C_D \rangle$ [-]	$C_{L,rms}$ [-]	St [-]
Case 1	1.01	0.09	0.21
Lysenko et al. (2012) TKE	0.97	0.09	0.209
Breuer (1998a)	1.016 - 1.486		0.215 +- 0.005
Franke and Frank (2002)	0.978 - 1.005		0.209
Ong and Wallace (1996)			0.21
Parnaudeau et al. (2008) LES			0.21
Prsic et al. (2012)	1.0996 - 1.2379	0.2279 - 0.4481	0.2054

One can see from Table 9.1 that the results are in agreement with the previous research. The difference in the value for $C_{L,rms}$ when comparing to Prsic et al. (2012) may be due to differences formation of the free shear layers from the cylinder surface according to Lysenko et al. (2012). When the boundary layer at the upper and lower parts of the cylinder surface detaches, free-shear layers are formed. Lysenko et al. (2012) pointed out that the location where transition from 2D to 3D flow takes place may affect the drag and lift forces. Also, it was stated that long and mainly two-dimensional free-shear layers may give a smaller variation of the of the drag and lift forces, and hence lower magnitude for $C_{L,rms}$. Lysenko et al. (2012) confirm that the more upstream the shear-layer transition occurs and vortices form, the shorter recirculation bubble length and higher amplitude of $C_{L,rms}$ is likely.

9.1.2 Statistics in the wake region

The flow is further analysed through velocity profiles in the cylinder wake. The velocity fields in the cylinder wake is presented through both the space- and time-averaged streamwise velocity component, u, and the space- and time-averaged crossflow velocity component, v.

To obtain the results averaged in space, the data are sampled in the XZ-plane, along 15 parallel lines extending from cylinder wall ($X/D = 0.5$) to $X/D = 10.5$ in the cylinder wake. The lines have 200 sampling points. The lines are distributed evenly along the cylinder span in Y = 0. The centreline mean streamwise velocity field is compared to what was found by Parnaudeau et al. (2008) and Wissink and Rodi (2008b) is are given in Figure 9.3.

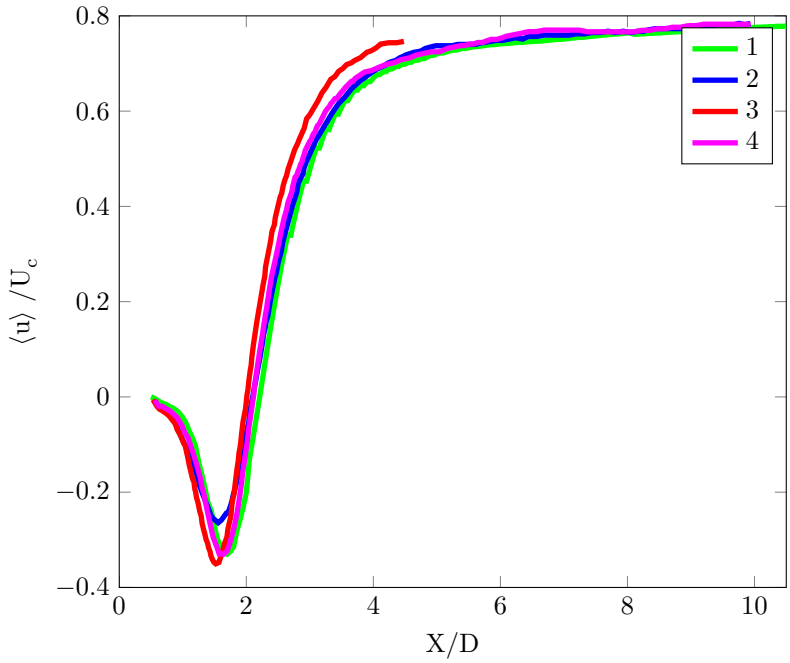

Figure 9.3: Mean streamwise velocity profile in the cylinder wake (Present 1 Case 1, 2 LES Parnaudeau et al. (2008), 3 PIV Parnaudeau et al. (2008), 4 Wissink and Rodi (2008b))

The mean recirculation zone length L_r corresponds to the distance between the base of the cylinder and the sign change of the centreline mean streamwise velocity. From Figure 9.3, one can see that the recirculation zone length is a bit longer for the present Case 1. L_r/D is found to be 1.7 in Case 1, which is in fairly good agreement with what was found by Lysenko et al. (2012) and Wissink and Rodi (2008b) ($L_r/D = 1.67$ for both).

The flow is also analysed in the YZ-plane, in three vertical cross-sections. The cross-sections are located in X/D = 0.53, 0.77 and 1.01, which are the same locations applied by Prsic et al. (2012). The velocity was sampled along 15 lines distributed evenly in the spanwise direction. The lines have 120 sampling points and extend from $Y/D = -3$ to $Y/D = 3$. Lysenko et al. (2012) and Parnaudeau et al. (2008) analysed the flow in the wake of the cylinder, starting at $X/D = 1.06$. Comparison

are made with the results from Lysenko et al. (2012) and Parnaudeau et al. (2008) at $X/D = 1.01$.

Figure 9.4 show the velocity fields in the streamwise direction at $X/D = 0.53$, 0.77 and 1.01.

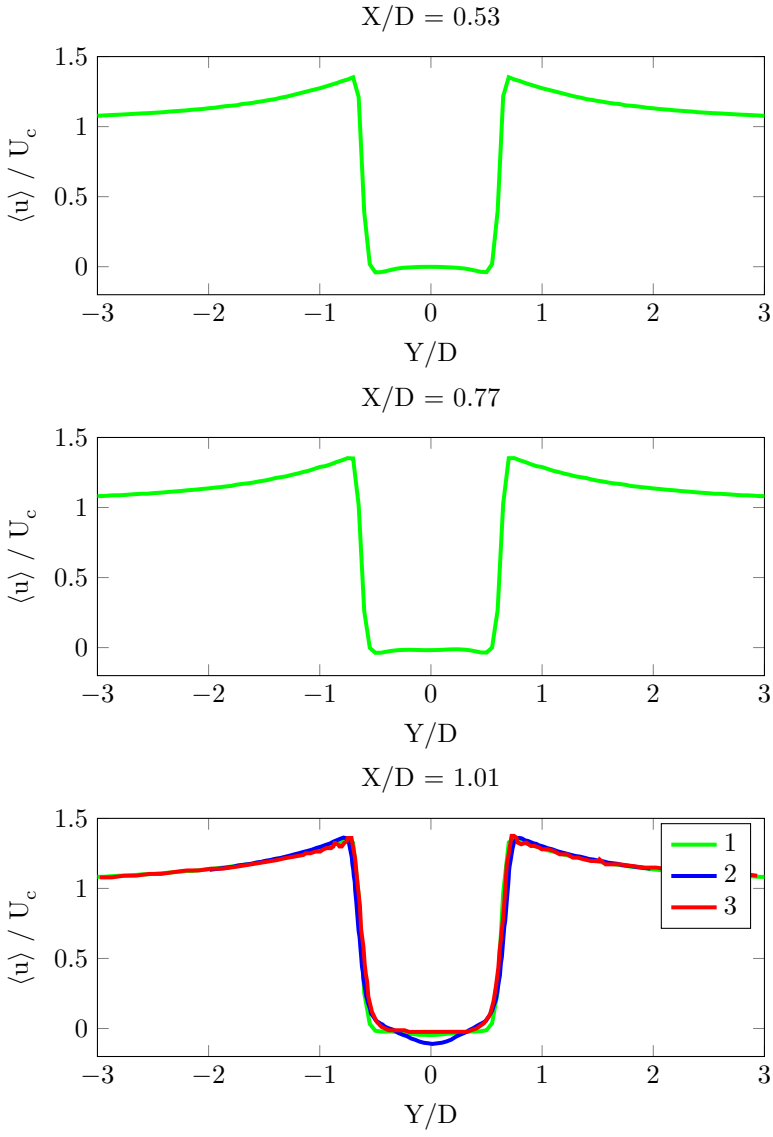

Figure 9.4: Mean streamwise velocity profiles at X/D = 0.53, 0.77 and 1.01 (1 Present Case 1, 2 LES Parnaudeau et al. (2008), 3 TKE Lysenko et al. (2012))

From Figure 9.4 one can see that the flow develops towards a U-shape downstream in the wake for Case 1. This is in good agreement with what was found by Lysenko et al. (2012) and Parnaudeau et al. (2008). The velocity is likely to develop against a V-shape further downstream. Prsic et al. (2012) obtained a V-shape at X/D = 1.01, and this illustrates the variety in results for this benchmark case as well as the possibility of the flow bifurcation as described by Lysenko et al. (2012).

Figure 9.5, show the velocity fields in the crossflow direction at $X/D = 0.53$, 0.77 and 1.01.

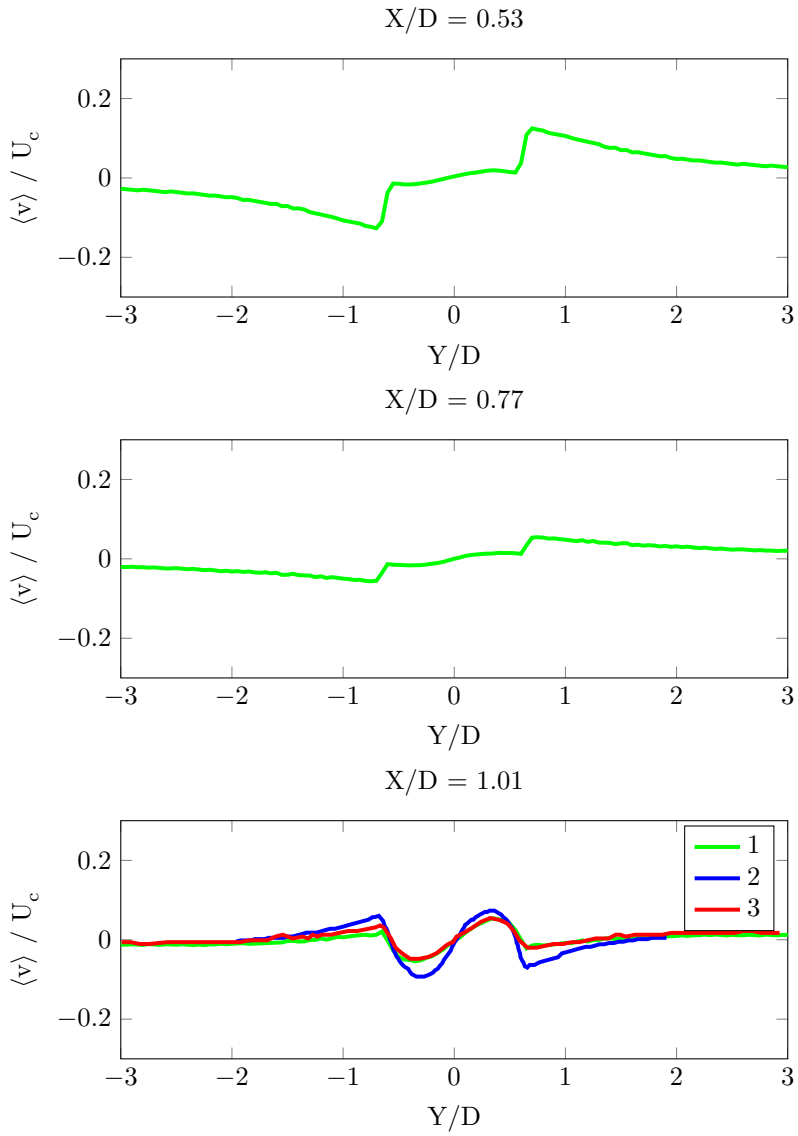

Figure 9.5: Mean crossflow velocity profiles at X/D = 0.53, 0.77 and 1.01 (1 Present Case 1, 2 LES Parnaudeau et al. (2008), 3 TKE Lysenko et al. (2012))

One can see from Figure 9.5 that the crossflow velocity profile is dominated by a wave around the origin of the cylinder, and symmetric extremal points at $Y/D = \pm 0.6$. The extrema remain at $Y/D = \pm 0.6$ with increasing X/D. However, the magnitude for $\langle v \rangle$ at the extrema decrease with increasing X/D. For the wave

around the origin, the magnitude remains as X/D is increased towards 1.01. It is expected that with further increased X/D in the wake, the wave will die out, the extrema at $X/D = \pm 0.6$ will remain, and the absolute value for $\langle v \rangle$ will increase before in dies out. This was observed by Lysenko et al. (2012) and Parnaudeau et al. (2008). The velocity profile in the crossflow direction almost coincide with the results obtained by Lysenko et al. (2012) and are in agreement with those obtained by Parnaudeau et al. (2008). According to Abrahamsen-Prsic (2013), this is the most sensitive parameter, and hence the results are considered satisfying.

9.1.3 Conclusion for Case 1

For Case 1, the results are in agreement with published research. Due to this, it is concluded that the numerical parameters were sufficient. The analysis encapsulates the physics of the flow around the circular cylinder subjected to Reynolds number 3900, and STAR-CCM+ is thus considered to be a sufficient software system in this case. An interesting outcome was the U-shaped streamwise velocity profile in the wake. Lysenko et al. (2012) obtained this with a TKE SGS model and not when applying the classic Smagorisky SGS model. However, in this thesis the U-shaped velocity profile was obtained with the Smagorinsky SGS model. This is very interesting.

9.2 Mesh Convergence study for Case 2a

Also for Case 2, the results are analysed through the time- and space-averaged standard hydrodynamic parameters of drag and lift coefficient. The results are given as mean drag coefficient, $\langle C_D \rangle$, and mean lift coefficient, $\langle C_L \rangle$, and can be seen in Figure 9.6. Because of the very small variations in $C_{L,rms}$ for each mesh, it is not presented in these results, and hence also St is not presented.

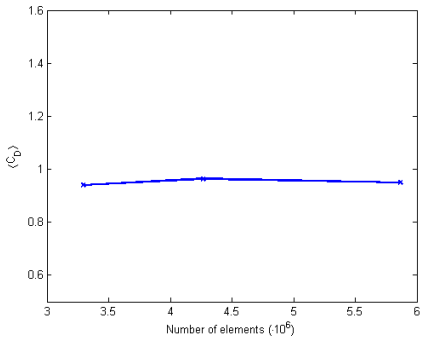

(a) $\langle C_D \rangle$ with respect to number of elements in the mesh

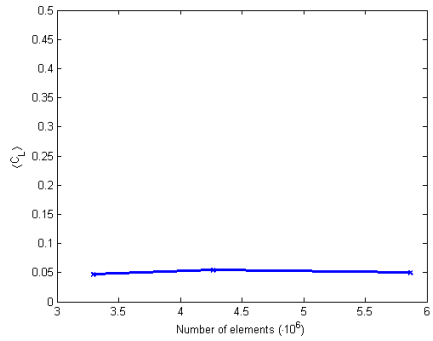

(b) $\langle C_L \rangle$ with respect to number of elements in the mesh

Figure 9.6

One can see from Figure 9.6 that the values for $\langle C_D \rangle$ and $\langle C_L \rangle$ are fairly constant. They do not increase or decrease linearly with the increase of elements in the grids. This may be due to that the solution is already converged. Also, a convergence is not always linear, the values may oscillate. The results are also given in Table 9.2.

Table 9.2: Mean flow parameters for Case 2a

Case	$\langle C_D \rangle$ [-]	$\langle C_L \rangle$ [-]
Case 2a_1	0.94	0.05
Case 2a_2	0.96	0.05
Case 2a_3	0.95	0.05

Similar to Case 1, the results are further analysed in the cylinder wake. The velocity field is sampled in the XZ-plane, along 15 parallel lines extending from the cylinder wall to X/D = 8 with 160 sampling points. The lines are distributed evenly along the cylinder span. Figure 9.7 show the streamwise velocity component averaged over the cylinder span.

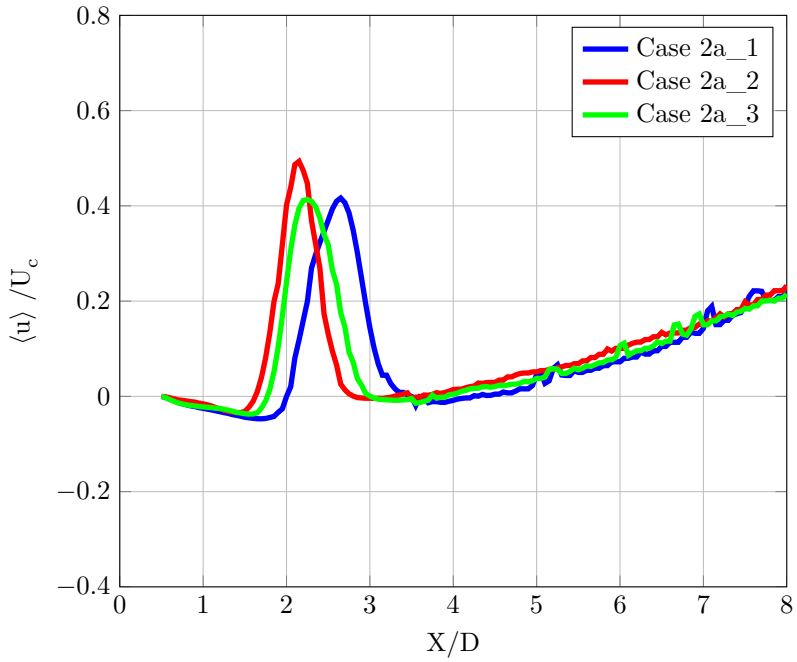

Figure 9.7: Mean streamwise velocity profile in the cylinder wake for the mesh convergence study

As for the mean drag coefficient and mean lift coefficient, it may be difficult to se a trend from the results in Figure 9.7. From Case 2a_1 to Case 2a_3, the recirculation length are decreasing with 15.3 %. The difference in recirculation length is smaller for Case 2a_3 and Case 2a_2. Based on the small differences in $\langle C_D \rangle$ and $\langle C_L \rangle$, the small difference in percentage decrease of L_r, and the computational time, Case 2a_2 is considered to be sufficiently resolved.

9.3 Comparison of Case 1, Case 2a and Case 2b

When comparing Case 1, Case 2a and Case 2b, the results for Case 2a_2 are chosen from Case 2a. This is because of the mesh convergence and also the fact that it is sufficient not to vary more than one parameter at a time.

9.3.1 Vortex shedding

As mentioned in section 2.3, since the e/D-ratio is less than the critical gap ($(e/D)_{crit} = 0.3$), the vortex shedding is expected to be suppressed. This was

experienced for $e/D = 0.2$ by Abrahamsen-Prsic et al. (2013). Lei et al. (1999) observed that the vortex shedding was suppressed at a gap-to-diameter ratio of about 0.2 - 0.3, depending on the boundary layer thickness. According to Zdravkovich (2009), the flow can be jet-like along the seabed due to the narrow gap. It was observed by Lei et al. (1999) that the critical gap ratio (for vortex shedding suppression) decreases as the thickness of the boundary layer decreases. Due to the very small variations in drag and lift for both Case 2a and Case 2b, it is concluded that the vortex shedding is suppressed as expected, and thus the Strouhal number is not calculated.

9.3.2 Mean flow parameters

Drag and lift

With suppressed vortex shedding, the variations for C_L and the mean value for $C_{L,rms}$ should be small for $e/D = 0.2$. Lei et al. (1999) observed that both drag and lift coefficients are dominated by the gap ratio and that the drag coefficient was slightly greater for the thinner boundary layers than in the thicker boundary layers at small gap ratios. Abrahamsen-Prsic et al. (2013) and Price et al. (2002) observed that the influence of the wall proximity maintains strong for small e/D ratios, but for $e/D > 1$ it was insignificant. Thus for $e/D > 1$, the flow behaves similar to Case 1. Lei et al. (1999) observed this for $e/D > 2$. Zdravkovich (1985) observed that also the lift coefficient depended strongly on the e/D ratio.

Lei et al. (1999) observed that the drag is almost unaffected by the gap ratio when the cylinder is out of the boundary layer. For a cylinder fully or partly immersed in the boundary layer, the drag coefficient increased with the ratio of the gap to the boundary layer thickness (e/δ). According to Zdravkovich (1985), the drag coefficients starts to decrease once the cylinder is immersed in the boundary layer, and the relevant parameter to describe the change of drag coefficient is e/δ. It was observed that the drag was reduced for $e/\delta < 1$. Thus it is expected that for Case 2a, where the cylinder is partly immersed in the boundary layer, that the drag coefficient will be of smaller magnitude than for Case 2b. Zdravkovich (1985) also observed that $\langle C_L \rangle$ varies with the type of boundary layer. The results for the comparison of Case 2a and Case 2b can be seen in Table 9.3.

Table 9.3: Mean flow parameters for Case 1, Case 2a and Case 2b

Case	$\langle C_D \rangle$ [-]	$\langle C_L \rangle$ [-]
Case 1	1.01	0
Case 2a_2	0.96	0.05
Case 2b	1.01	0.09

From Table 9.3, one can see that for Case 2a, $\langle C_D \rangle$ decreased with 0.05 compared to

Case 1, and a decrease was expected. The magnitude for the mean drag coefficient for Case 2a with no boundary layer thickness is equal to the drag coefficient in Case 1, where the cylinder is in infinite stream. This coincides with the observations from Lei et al. (1999) and Zdravkovich (1985), i.e the drag coefficient is unaffected by the proximity of the wall when the cylinder is not submerged in the boundary layer. Another interesting result is the mean lift coefficient. It is of higher magnitude for Case 2b than for Case 2a, almost double. As mentioned in section 2.5.2, the introduction of shear flow, will not make the stagnation point move significantly, but the stagnation pressure will drop. This was further investigated through the pressure distribution around the cylinder wall.

Pressure coefficient

It was observed by Abrahamsen-Prsic et al. (2013) that a thicker boundary layer leads to a less pronounced maximum in C_P, and a less negative base pressure. The difference was observed to be greatest between the case were the cylinder was completely out of the boundary layer, and the cases where the cylinder was partially and fully immersed in the boundary layer shear flow. The same effect was also observed by Lei et al. (1999). The time- and space-averaged pressure coefficients are found for both Case 1, Case 2a and Case 2b. The data was sampled along 15 lines distributed evenly in the spanwise direction around the cylinder wall. The variations for the pressure coefficients for both Case 1, Case 2a and Case 2b can be seen in 9.8.

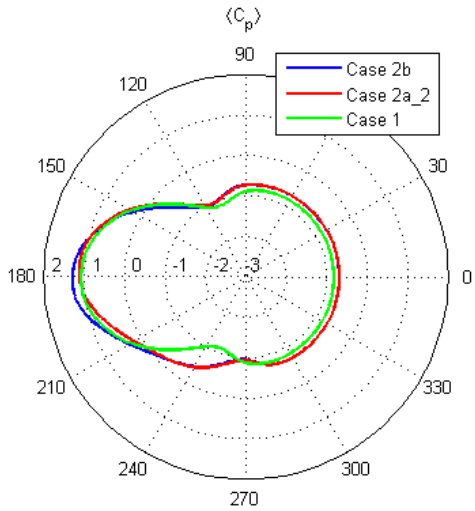

Figure 9.8: Mean pressure distribution at the cylinder surface for the different cases

As expected, the stagnation pressure is of higher magnitude for Case 2b with uniform inflow velocity profile than for Case 2a. This may thus explain the higher $\langle C_L \rangle$ for Case 2b. Also, the stagnation point does not move significantly from Case 2a to Case 2b. It can be seen from the figure that the base pressure is of lower magnitude for Case 1 that for the remaining cases. The higher base base pressure for Case 2 is caused by the proximity of the wall. The stagnation only moves slightly for Case 2a and Case 2b compared to Case 1.

9.3.3 Statistics in the wake region

The results are further analysed in the cylinder wake. The streamwise velocity field is sampled in the XZ-plane, along 15 parallel lines extending from the cylinder wall to X/D = 8 with 160 sampling points. The lines are distributed evenly along the cylinder span. Figure 9.9 show the streamwise velocity component u averaged over the cylinder span for Case 2a and Case 2b.

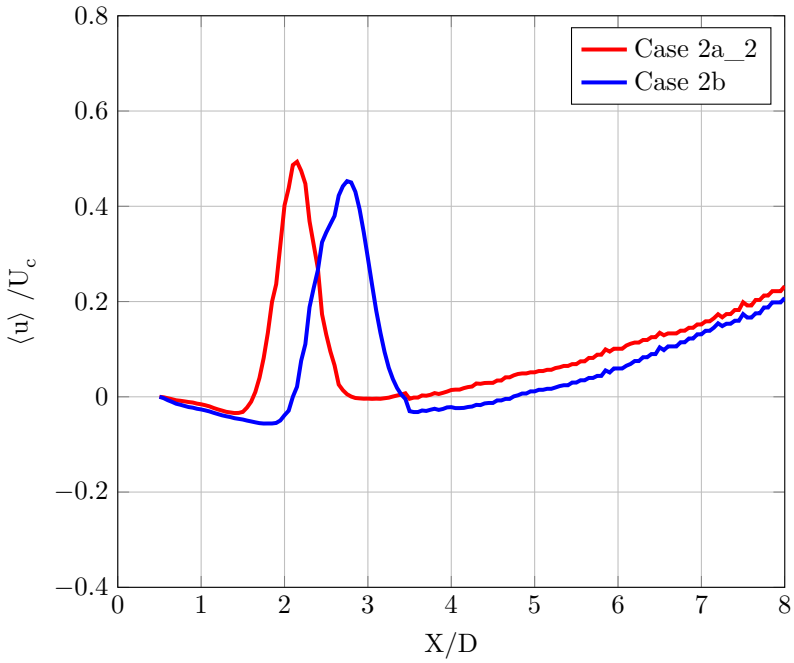

Figure 9.9: Mean streamwise velocity profile in the cylinder wake for Case 2a and Case 2b

From Figure 9.9, it can be seen that the recirculation zone length is longer for Case 2b than for Case 2a. For Case 2a, the recirculation length equal to $1.125 \cdot D$. For Case 2b, the recirculation zone length is equal to $1.6 \cdot D$. The difference is almost

30 %, which is significant.

The flow is also analysed in the YZ-plane in 5 vertical cross-sections. The cross sections are located from the cylinder centreline at $X/D = 0$ to $X/D = 6$. The data was sampled along 15 lines distributed evenly in the spanwise direction for each cross-section. The lines have 100 sampling points and extend from $Y/D = -0.7$ to $Y/D = 4$. The streamwise velocity fields for Case 2a and Case 2b are compared and can be seen in Figure 9.10.

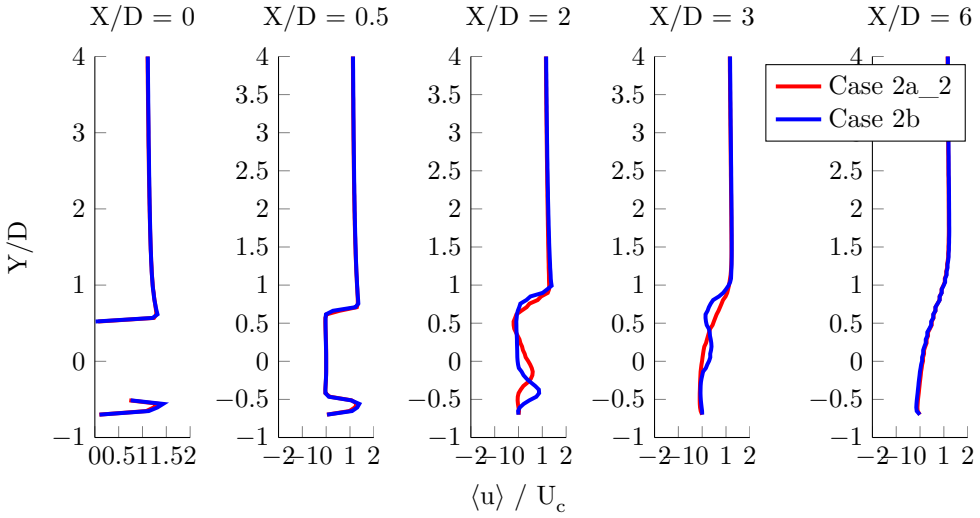

Figure 9.10: Mean streamwise velocity profiles at X/D = 0, 0.5, 2, 3 and 6

From Figure 9.10 it can be seen that for $X/D = 2$, 3 and 6 there is a the streamwise velocity decreases behind the cylinder. A decrease was also observed by Abrahamsen-Prsic et al. (2013) for $e/D = 0.2$ with a $\delta/D = 1.6$. Abrahamsen-Prsic et al. (2013) studied to flow for Re = 13100. The flow regime is equal, and thus the flow is considered to behave qualitatively similar. A decrease in the streamwise velocity was observed by Sarkar and Sarkar (2010) for $e/D = 0.25$ in the range of $X/D = 2$ to $X/D = 3$ for $Re = 1440$. This was attributed to the coupling between the inner shear layer and the boundary layer. Oner et al. (2008) measured the the streamwise velocity for different cross flow sections between $X/D = -1.5$ and $X/D = 1.5$ for $e/D = 0.2$ and $Re = 9500$. For both Case 2a and Case 2b, the flow is observed to behave qualitatively equal to what was observed by Sarkar and Sarkar (2010), Abrahamsen-Prsic et al. (2013) and Oner et al. (2008).

It is of interest to see how the Case 2a and Case 2b develop different from each other downstream in the wake. The meantioned decrease occurs closer to the cylinder for Case 2a than for Case 2b. This must be seen in context with the recirculation zone length for both cases. The larger recirculation zone length for Case 2b confirms this effect.

The two velocity profiles were also investigated in front of the wake at $X/D = -1$ and $X/D = -3$, see Figure 9.11.

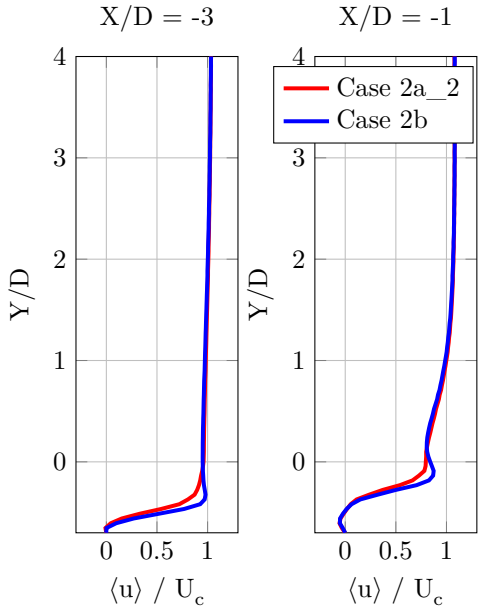

Figure 9.11: Mean streamwise velocity profiles at X/D = -0.1 and -0.3

The differences in the velocity profiles in front of the cylinder are seen clearly. Case 2b has higher streamwise velocity for low Y/D than Case 2a. This was expected due to the delay of Case 2b compared to Case 2a in the cylinder wake.

9.3.4 Conclusion for Case 2

The influence of a near-bed flow over a circular cylinder has been investigated and the results are interesting. Both for Case 2a and Case 2b, the vortex shedding was suppressed as expected. Case 2a was set up with a boundary layer thickness of $\delta/D = 0.48$. The boundary layer which exposes the cylinder to shear flow, affect the drag coefficient, and cause causes it to decrease. The vicinity of the wall is causing the lift coefficient to be fairly positive for both cases. However, the lift coefficient for Case 2b is of higher magnitude. This is likely to be caused by the higher pressure in the stagnation point. Also, for Case 2, the magnitude of the drag coefficient is approximately equal to the drag coefficient in Case 1, where the cylinder is subjected to free stream. Hence, according to these analyses, the inlet velocity profile is of importance. Looking at the velocity profiles in the wake for Case 2, the differences between Case 2a and Case 2b can be seen clearly. The

recirculation length is larger for Case 2b. The changes in the velocity profiles in the wake are observed further downstream for Case 2b than for Case 2a.

9.4 Sources of error

In order to achieve successful results, the CFD-code must be applied in a fair manner. In other words, the code should be used for problems it may simulate well.

Mesh

Without a sufficient mesh, the equations which are to be solved may not be discretized successfully in space. In this thesis, the mesh generation is based on previously mentioned research. However, one may note that the mesh is refined more in XY-plane than in the spanwise direction. Also, the mesh convergence study did not investigate the spanwise resolution. To few elements in Z-directions may reduce the quality of the results. Still, due to small differences in the mesh convergence study for Case 2a and the results for Case 1, the mesh is considered to be sufficiently resolved.

Time step

The time step decides the discretization of the equations in time. The size of the time step used in this thesis is based on the previously mentioned studies. However, a time step convergence analysis should be performed to ensure that the time step was small enough for this application of the CFD code. Due to limited time, this was not accomplished.

Discretization schemes

The accuracy of the discretization schemes for both space and time was proven to affect the results by Breuer (1998a). Not all types of schemes are sufficient for LES. In this thesis, the applied schemes are recommended by CD-adapco (2013). Other schemes may be sufficient.

Number of iterations per time step

In all analyses 16 iterations per time step was utilized. According to Support, CD-adapco - Star-CCM+ (2013), the time step was converged (see section 6.2). However, the residuals did not converge to the same order of magnitude as they did for Abrahamsen-Prsic et al. (2013); Prsic et al. (2012).

Statistical sampling time

In this thesis, the statistics were sampled for 50 vortex shedding periods. Franke and Frank (2002) concluded that more than 40 vortex shedding cycles was necessary to obtain a converged mean flow statistics. Parnaudeau et al. (2008) and Prsic et al. (2012) collected data of about 60 vortex shedding cycles. Lysenko et al. (2012) sampled the statistics over 150 vortex shedding periods in order to ensure statistical convergence. 50 vortex shedding cycles may not be enough, but due to limited time, the statistics could not be sampled for a longer time.

Chapter 10

Review of STAR-CCM+

One of the challenges in this thesis, was the attempt of using STAR-CCM+ to approach the scope of work. The commercial sofware ANSYS Fluent and also the open source code OpenFOAM, has been applied within the Department of Marine Technology at NTNU for similar problems. In this chapter, the gained knowledge regarding STAR-CCM+ for these type of problems is discussed. Hopefully, the next students at NTNU applying STAR-CCM+ for similar problems will have a more effective start.

10.1 Preprocessing

The simulation topology is briefly explained in [Thingbø, 2012]. Learning to set up an analysis using STAR-CCM+ was quite easy once accomplished once or twice, because STAR-CCM+ has a good user interface. STAR-CCM+ provides useful tutorial guides for setting up simulations and meshing. However, there were no tutorials available for LES simulations, which was a bit peculiar. One would think that CD-adapco would have accomplished a successful LES simulation and thus make it available for the users of STAR-CCM+. This is not the case, and setting up a simulation from scratch without any guidance from tutorials will take time for a beginner. Luckily, in this thesis the experience from [Thingbø, 2012] could be applied to some extent.

Regarding meshing in STAR-CCM+, one can use both structured and unstructured meshes. However, the meshing can not be done by any other kind of preprocessor, because not all formats are accepted by STAR-CCM+. In [Thingbø, 2012], the mesh was prepared by using the unstructured mesh modules in STAR-CCM+. In the master thesis, the mesh was prepared by using the directed mesher in STAR-CCM+ which gives a structured mesh. The structured mesh was experienced to give much higher degree of control over the meshing when used for the simple

geometry of Case 1 and Case 2. The structured meshing option in STAR-CCM+ was greatly improved by CD-adapco during the semester for the thesis. Before the improvements, it did not give sufficiently control over the patch curves (see section 4.1), and hence was not an option for meshing at all. For more complex geometries a structured mesh will probably be too time consuming, and thus it can not be recommended. The unstructured meshing alternatives in STAR-CCM+ are instead recommended for such geometries.

10.2 Running simulations

In STAR-CMM+, one can run the simulation to a given stopping criteria (for transient simulations: a specified physical time). The simulations is then saved, and changes in the simulation file can be made before running the simulation further to a new stopping criteria. The simulation will then use the so-far-obtained solution when it starts running again. Examples of successful changes tested during this thesis are

- Changing the time step
- Changing number of iterations per time step
- Generating a new mesh. The so-far-obtained solution is then interpolated to the new mesh before further running.
- Changing boundary conditions, e.g velocity at the inlet boundary.
- Changing the frequency for saving the solution to the history file and also changing the solution history file.

One should note that it is not possible to change the computational domain. Other than this, many variables may be changed in STAR-CCM+ and this is very useful.

10.3 Postprocessing

During the thesis, a large amount of time was spent on finding the right data for evaluating the results. Parameters like drag and lift coefficients are not difficult to obtain from the simulations in STAR-CCM+. However, the details of the wake, i.e the velocity profiles are more difficult to find. This was frustrating, because the results are of course somewhere in the solution file, but they are not that easily "available" for the user. Or to explain this in an other manner, STAR-CCM+ did not advertise the tutorials for finding this, and support had problems understanding why velocity profiles were of relevance. STAR-CCM+ is applied for many types of problems, e.g for the car industry and air craft industry. Thus, it is not specialized for marine related problems. What is mostly advertised for and explained in tutorials are the colourful scenes and animations. However, these do

not give much detail and are not necessarily of great value for this type of problem in a report.

10.3.1 Averaging in time and space

For this thesis, it was preferred that the results were averaged over the spanwise direction. In STAR-CCM+, a field function called the *coordinate system averaging* field function could have been applied. However, this field function should only be applied for axis-symmetric geometries. Because the cylinder is not placed in the centre of the computational domain for neither Case 1 nor Case 2, support could not guarantee good results with this field function. [Support, CD-adapco - Star-CCM+, 2013] Due to this limitation, the field function was not applied. Instead the averaging over the cylinder was accomplished by creating several probe lines distributen in the spanwise direction. This is further explained in Chapter 5 and Chapter 9. If the coordinate system averaging field function could have been applied, it would have saved a lot of time during the postprocessing.

So called *field mean monitors* were applied in order to gain statistics for velocity profiles, pressure coefficients, and velocity contour lines averaged over time. Unfortunately, these monitors are not as flexible as one could expect. In the settings for each monitor, one must decide at which frequency the data should be sampled. The monitors are not able to store the sampled data and calculate the average with a lower frequency. For turbulent flows, the data should be sampled each time step, and thus the calculated averages must also be made for each time step in STAR-CCM+. With many monitors, the computational time increased tremendously. If the monitors could save the sampled data and calculate the time averaged data with a lower frequency, this would save computational time. Since this is not possible in STAR-CCM+, the user must select the data for postprocessing carefully.

After the simulations have finished and the field mean monitors have been used to gather statistics, plots of the different data are easy to achieve in STAR-CCM+. Assuming that the user is familiar with derived parts (explained by Thingbø (2012)), then for example time averaged velocity profiles are quickly created. All plots created in STAR-CCM+ can be exported and imported into MATLAB. This has been very useful for further postprocessing and comparison.

Although not all preprocessing and postprocessing information needed was easy to find, most information could be found by using support actively. However, one should have in mind that the support for STAR-CCM+ are not necessarily specialised for the physics in these cases. Some times a huge amount of e-mails are needed to find what is considered both necessary and elementary information and results for marine engineers.

Chapter 11

Conclusion

In this master thesis, the flow around a circular cylinder at $Re = 3900$ has been investigated using 3D LES. The software system STAR-CCM+ is used for all analyses. Three different cases have been analysed.

- Case 1 describes a cylinder in uniform, steady and infinite current, which is a benchmark case. The results are considered to be in agreement with previous studies carried out by numerical models and also experiments. From this it is concluded that the STAR-CCM+ software system performs well using LES and the Smagorinsky subgrid scale turbulence model for Case 1. The flow in the boundary layers on the cylinder, the two shear layers delimiting the recirculation region and the near wake is successfully simulated.
- Case 2a describes a cylinder in the vicinity of a rigid wall, with a inlet boundary layer profile with a thickness of $\delta = 0.48 \cdot D$. The gap-to-diamter thickness is 0.2. For Case 2a it is observed that the vortex shedding was suppressed with a e/D-ratio of 0.2. The mean lift coefficient was increased and the mean drag coefficient was decreased compared to Case 1.
- Case 2b is equal to the Case 2a, except of an uniform inlet velocity. As for Case 2a it is observed that the vortex shedding was suppressed. The mean lift coefficient was increased and of higher magnitude than Case 2a. The drag coefficient was of same magnitude as it was for Case 1.

It was investigated how the gap-to-diameter ratio and the boundary layer thickness affect the flow around the cylinder. It was observed that due to the differences in the inlet velocity for Case 2a and Case 2b, the wake statistics was affected. Hence, Case 2a and Case 2b have illustrated that both the inlet velocity and the proximity of a rigid wall indeed affect the flow around the cylinder and the forces acting on it.

Chapter 12

Further Work

When using CFD, many parameters can be investigated. Further work with this thesis has great potential when it comes to developing new knowledge of physics regarding a cylinder in flow.

- The sampling of data should continue for a larger number of vortex shedding periods. By doing so, the statistical convergence could be consolidated. In order to check whether the number of inner iterations are sufficiently, the analyses should be accomplished with increased number of iterations per time step. The results should then be compared to what is found in this thesis.
- For Case 1, the influence of time step and mesh resolution are convergence studies of interest. Due to limited time, this was not investigated in this thesis, but would be a natural approach in the further work. The highest priority for further work with Case 2 is to run another case in the mesh convergence study. Due to the small variations in the hydrodynamical parameters and the streamwise velocity profile, the case should be simulated with a coarser mesh. In this way it could be concluded whether convergence is really obtained. In addition, Case 2 can be varied in many ways. The influence of e/D and δ/D could be investigated in a larger extent. Other types of flow, for example oscillating flows can be instructive. Analyses on a cylinder at a higher Reynolds number will introduce new physics, and seabed scour is also a topic of interest.
- Other software can been used in order to see the difference between the application of Star-CCM+ and the alternatives. This master thesis has mostly focused on the physics of the problem. For a better understanding of the numerical aspect, discretization schemes and solvers should be studied thoroughly.

Chapter 13

References

Abrahamsen-Prsic, M. (2013). Conversations. January - June.

Abrahamsen-Prsic, M., Ong, M. C., Pettersen, B., and Myrhaug, D. (2013). Large eddy simulation of flow around a circular cylinder in the vicinity of a wall at Reynolds number of 13100. Not published.

Breuer, M. (1998a). Large eddy simulation of the subcritical flow past a circular cylinder: numerical and modeling aspects. *International Journal for Numerical Methods in Fluid*, Vol. 28:pp. 1281–1302.

Breuer, M. (1998b). Numerical and modeling influences on large eddy simulations for the flow past a circular cylinder. *International Journal of Heat and Fluid Flow*, Vol. 19:pp. 512–521.

CD-adapco (2013). *User Guide - Star-CCM+ Version 8.02*.

Ferziger, J. H. and Peric, M. (1997). *Computational Methods for Fluid Dynamics*. Springer-Verlag.

Franke, J. and Frank, W. (2002). Large eddy simulation of the flow past a circular cylinder at ReD = 3900. *Journal of Wind Engineering and Industrial Aerodynamics*, Vol. 90:pp. 1191–1206.

Lei, C., Cheng, L., Armfield, S. W., and Kavanagh, K. (2000). Vortex shedding suppression for flow over a circular cylinder near a plane boundary. *Ocean Engineering*, Vol. 27:pp. 1109–1127.

Lei, C., Cheng, L., and Kavanagh, K. (1999). Re-examination of the effect of a plane boundary on force and vortex shedding of a circular cylinder. *Journal of Wind Engineering and Industrial Aerodynamics*, Vol. 80:pp. 263–286.

Li, Y. (2011). Large eddy simulation of flow around a cylinder at Re=3900 using a CFD code. *Applied Mechanics and Materials*, Vols. 94-96:pp. 1707–1710.

Lysenko, D. A., Ertsvåga, I. S., and Rian, K. E. (2012). Large-Eddy Simulation of the flow over a circular cylinder at Reynolds number 3900 using the OpenFOAM Toolbox. *Flow Turbulence Combust*, Vol. 89:pp. 491–518.

Ma, X., Karamanos, G.-S., and Karniadakis, G. E. (2000). Dynamics and low-dimensionality of a turbulent near wake. *J. Fluid Mech.*, Vol. 410:pp. 29–65.

NTNU HPC GROUP (2012). About Vilje. `https://www.hpc.ntnu.no/display/hpc/About+Vilje#`.

Oner, A. A., Kirkgoz, M. S., and Akoz, M. S. (2008). Interaction of a current with a circular cylinder near a rigid bed. *Ocean Engineering*, Vol. 35:pp. 1492–1504.

Ong, L. and Wallace, J. (1996). The velocity field of the turbulent very near wake of a circular cylinder. *Experiments in Fluid*, Vol. 20:pp. 441–453.

Ong, M. C., Utnes, T., Holmedal, L. E., Myrhaug, D., and Pettersen, B. (2008). Numerical simulation of flow around a marine pipeline close to the seabed. In *Proceedings of the* 31^{st} *International Conference on Coastal Engineering*.

Ong, M. C., Utnes, T., Holmedal, L. E., Myrhaug, D., and Pettersen, B. (2010). Numerical simulation of flow around a circular cylinder close to a flat seabed at high Reynolds numbers using a k-ϵ model. *Costal Engineering*, Vol. 57:pp. 931–947.

Parnaudeau, P., Carlier, J., Heitz, D., and Lamballais, E. (2008). Experimental and numerical studies of the flow over a circular cylinder at Reynolds number 3900. *Physics of Fluid*, Vol. 20:085101.

Price, S. J., Sumner, D., Smith, J. G., Leong, K., and Paidoussis, M. P. (2002). Flow visualization around a circular cylinder near to a plane wall. *Journal of Fluids and Structures*, Vol. 16:pp. 175–191.

Prsic, M., Ong, M. C., Pettersen, B., and Myrhaug, D. (2012). Large Eddy Simulations of three dimensional flow around a pipeline in a uniform current. In *Proceedings of the 31st International Conference on Ocean, Offshore and Arctic Engineering*.

Sarkar, S. and Sarkar, S. (2010). Vortex dynamics of a cylinder wake in proximity to a wall. *Journal of Fluids and Structures*, Vol. 26:pp. 19–40.

Sumer, B. M. and Fredsøe, J. (1997). *Hydrodynamics around Cylindrical Structures*. World Scientific Publishing Co. Pte. Ltd.

Support, CD-adapco - Star-CCM+ (2013). E-mail correspondence.

Thingbø, S. S. (2012). Calculation of Vicous Flow around a Circular Cylinder.

Tremblay, F., Manhart, M., and Friedrich, R. (2000). LES of flow around a circular cylinder at a subcritical Reynolds Number with cartesian Grids. *Advances in LES of Complex Flows*, pages pp. 133–150.

Wang, X. K. and Tan, S. K. (2008). Near-wake flow characteristics of a circular cylinder close to a wall. *Journal of Fluid and Structures*, Vol. 24:pp. 605–627.

White, F. M. (2006). *Viscous Fluid Flow*. McGraw Hill.

Wissink, J. G. and Rodi, W. (2008a). Large-scale computations of flow around a circular cylinder. *High Performance Computing on Vector Systems*, pages pp. 71–81.

Wissink, J. G. and Rodi, W. (2008b). Numerical study of the near wake of a circular cylinder. *International Journal of Heat and Fluid Flow*, Vol. 29:pp. 1060–1070.

Zdravkovich, M. M. (1985). Forces on a circular cylinder near a plane wall. *Applied Ocean Research*, Vol. 7 (4):pp. 197–201.

Zdravkovich, M. M. (2009). *Flow around circular cylinder. Vol 2: Applications*. Oxford University Press.

Appendix A

The Navier-Stokes equations

The following can be found in [White, 2006].

There are three basic laws for of conservation for a physical system:

1. Conservation of mass (continuity)
2. Conservation of momentum (Newton's second law)
3. Conservation of energy (first law of thermodynamics)

The three unknowns that can be obtained from these equations are the velocity $\vec{V}$, the thermodynamic pressure p, and the absolute temperature T. p and T are considered to be the two required independent thermodynamic variables. However, the final forms of the conservation equations also contain four other thermodynamic variables: the density ρ, the enthalpy h (for the internal energy e), and the two transport properties μ and k. By using the assumption that the latter four properties are determined by the values of ρ and T, the following yields

$$\begin{aligned} \rho &= \rho(p,T) \qquad h = h(p,T) \\ \mu &= \mu(p,T) \qquad k = k(p,T) \end{aligned} \tag{A.1}$$

These variables can be found in tables or charts or by semiteoretic formulas from kinetic theory. The fluid is assumed to be of uniform, homogeneous composition, i.e., diffusion and chemical reactions are not considered.

A.1 Conservation of Mass

The particle derivative is given by

$$\frac{D}{Dt} = \frac{\partial}{\partial t} + (\vec{V} \cdot \vec{\nabla}) \tag{A.2}$$

In Lagrangian terms, the law of conservation is simply

$$m = \rho\mathcal{V} = \text{const} \tag{A.3}$$

where $\mathcal{V}$ is the volume of a particle. Using Eulerian terms, this is equivalent

$$\frac{Dm}{Dt} = \frac{D}{Dt}(\rho\mathcal{V}) = 0 = \rho\frac{D\mathcal{V}}{Dt} + \mathcal{V}\frac{D\rho}{Dt} \tag{A.4}$$

$\frac{D\mathcal{V}}{Dt}$ can be related to the fluid velocity because the normal strain rate is equal to the rate of volume increase of a particle per unit volume:

$$\epsilon_{xx} + \epsilon_{yy} + \epsilon_{zz} = \frac{1}{\mathcal{V}}\frac{D\mathcal{V}}{Dt} \tag{A.5}$$

The strain rates can be substituted from kinematic relations:

$$\begin{aligned} \epsilon_{xx} + \epsilon_{yy} + \epsilon_{zz} &= \frac{\partial u}{\partial x} + \frac{\partial v}{\partial y} + \frac{\partial w}{\partial z} \\ &= \text{div}\vec{V} = \nabla \cdot \vec{V} \end{aligned} \tag{A.6}$$

By combining Eqs. A.4 - A.6, $\mathcal{V}$ can be eliminated, and the most general equation of continuity for fluids is obtained:

$$\frac{D\rho}{Dt} + \rho \text{ div } \vec{V} = 0 \qquad \text{or} \qquad \frac{\partial\rho}{\partial t} + \text{ div } \rho\vec{V} = 0 \tag{A.7}$$

If the density is constant (incompressible flow), Eq- A.7 reduces to

$$\text{div } \vec{V} = \frac{\partial u}{\partial x} + \frac{\partial v}{\partial y} + \frac{\partial w}{\partial z} = 0 \tag{A.8}$$

A.2 Conservation of Momentum

Newton's second law expresses the relation between an applied force and the resulting acceleration of a particle of mass m:

$$\vec{F} = m\vec{a} \tag{A.9}$$

When working with fluid particles, it is convenient to divide Eq. A.9 by volume, so that the equation is written in terms of density instead of mass. The acceleration is placed on the left side:

$$\rho\frac{D\vec{V}}{Dt} = \vec{f} = \vec{f_{body}} + \vec{f_{surface}} \tag{A.10}$$

where $\vec{f}$ is the applied force per unit volume on the fluid particle. The body forces are those that apply to the entire mass of the fluid element. Such forces are usually due to external fields, such as gravity or electromagnetic potential. If the magnetohydrodynamic forces are ignored and only the gravitational body force are considered, then on a unit volume

$$\vec{f_{body}} = \rho\vec{g} \tag{A.11}$$

where $\vec{g}$ is the vector acceleration of gravity.

Surface forces are applied by external stresses in the sides of the element. The quantity stress τ_{ij} is a tensor and the sign convention for the stress components on a Cartesian element can be seen in Figure A.1.

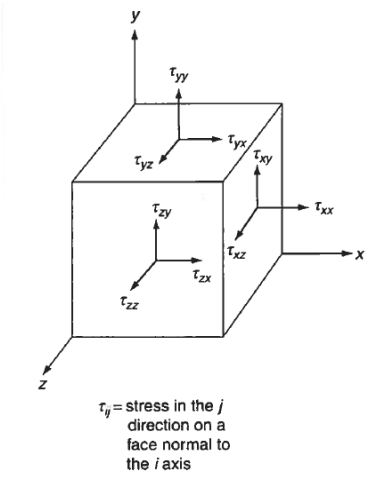

Figure A.1: Notation for stresses [White, 2006]

The stress tensor can be written as

$$\tau_{ij} = \begin{pmatrix} \tau_{xx} & \tau_{xy} & \tau_{xz} \\ \tau_{yx} & \tau_{yy} & \tau_{yz} \\ \tau_{zx} & \tau_{zy} & \tau_{zz} \end{pmatrix} \tag{A.12}$$

The tensor is symmetric such that $\tau_{ij} = \tau_{ji}$. By setting up the force equilibrium for the front faces of the element in Figure A.1, the vector surface force written with Einstein summation notation is obtained:

$$\vec{f_{sur}} = \vec{\nabla} \cdot \tau_{ij} = \frac{\partial \tau_{ij}}{\partial x_{ij}} \tag{A.13}$$

where the divergence of τ_{ij} is on tensor form, so that the result is a vector.

Newton's law can now be written

$$\rho \frac{D\vec{V}}{Dt} = \rho \vec{g} + \nabla \cdot \tau_{ij} \tag{A.14}$$

The stresses τ_{ij} is obtained by

$$\tau_{ij} = -p\delta_{ij} + \mu\big(\frac{\partial u_i}{\partial x_j} + \frac{\partial u_j}{\partial x_j}\big) + \delta_{ij}\lambda \text{ div } \vec{V} \tag{A.15}$$

For incompressible flow Eq. A.15 reduces to

$$\tau_{ij} = -p\delta_{ij} + \mu\big(\frac{\partial u_i}{\partial x_j} + \frac{\partial u_j}{\partial x_j}\big) \tag{A.16}$$

where δ_{ij} is the Kronecker delta, given by

$$\delta_{ij} = \begin{cases} 1 & \text{if } i = j \\ 0 & \text{if } i \neq j \end{cases} \tag{A.17}$$

The momentum equation for a general linear (newtonian) viscous fluid in now obtained by substituting the stress relations (Eq. A.16), into Newton's second law

(Eq. A.14). In scaler form the Navier-Stokes equations for incompressible flow are given by:

$$\rho\frac{Du}{Dt} = \rho g_x - \frac{\partial p}{\partial x} + \frac{\partial}{\partial x}\left(2\mu\frac{\partial u}{\partial x}\right) + \frac{\partial}{\partial y}\left[\mu\left(\frac{\partial u}{\partial y} + \frac{\partial v}{\partial x}\right)\right] + \frac{\partial}{\partial z}\left[\mu\left(\frac{\partial w}{\partial x} + \frac{\partial u}{\partial z}\right)\right]$$

$$\rho\frac{Dv}{Dt} = \rho g_y - \frac{\partial p}{\partial y} + \frac{\partial}{\partial x}\left[\mu\left(\frac{\partial v}{\partial x} + \frac{\partial u}{\partial y}\right)\right] + \frac{\partial}{\partial y}\left(2\mu\frac{\partial v}{\partial y}\right) + \frac{\partial}{\partial z}\left[\mu\left(\frac{\partial v}{\partial z} + \frac{\partial w}{\partial y}\right)\right]$$

$$\rho\frac{Dw}{Dt} = \rho g_z - \frac{\partial p}{\partial z} + \frac{\partial}{\partial x}\left[\mu\left(\frac{\partial w}{\partial x} + \frac{\partial u}{\partial z}\right)\right] + \frac{\partial}{\partial y}\left[\mu\left(\frac{\partial v}{\partial z} + \frac{\partial w}{\partial y}\right)\right] + \frac{\partial}{\partial z}\left(2\mu\frac{\partial w}{\partial z}\right) \tag{A.18}$$

If μ is assumed constant, the simpler *Navier-Stokes equation for constant viscosity and constant density* is achieved. The equation can be written as a single equation by using Einstein notation:

$$\rho\frac{D\vec{V}}{Dt} = \rho\vec{g} - \nabla p + \mu\nabla^2\vec{V} \tag{A.19}$$

One should note that for incompressible flow and constant viscosity the equation for conservation of mass (Eq. A.8) and the equation for conservation of momentum (Eq. A.19) are entirely uncoupled from temperature. This means that one can solve the continuity equation and the momentum equation for velocity and pressure and if desired, solve for temperature from the *energy equation* (which will not be further discussed here)